1	Distribution of extreme rainfall events and their environmental controls in the West African Sahel and
2	Soudan
3	
4	
5	Edward K. Vizy* and Kerry H. Cook
6	Department of Geological Sciences
7	Jackson School of Geosciences, The University of Texas at Austin
8	Austin, TX 78712
9	
10	
11	
12	February 8, 2022
13	Published in Climate Dynamics
14 15 16	This preprint has not undergone any post-submission improvements or corrections. The Version of Record of this article is published in Climate Dynamics, and is available online at https://doi.org/10.1007/s00382-022-06171-x
17	The citation for this work is as follows:
18 19 20 21 22	Vizy EK, Cook KH (2022) Distribution of extreme rainfall events and their environmental controls in the West African Sahel and Soudan. <i>Climate Dynamics</i> , 59, 997-1026. https://doi.org/10.1007/s00382-022-06171-x
23	* Corresponding author e-mail: ned@jsg.utexas.edu
24	

Abstract

West African Sahel and Soudan extreme rainfall events are impactful when strong mesoscale convective systems (MCSs) produce large amounts of rainfall in short periods. NASA IMERG rainfall estimates and the ERA5 reanalysis are examined to understand where the top 100 highest 12Z – 12Z 24-h rainfall totals and MCS storm genesis occur, and to assess the relative importance of environmental conditions in their generation including the influence of atmospheric moisture and vertical wind shear.

Most of the top 100 events are located south of 14°N over the Soudan. Events cluster over three regions, namely, Mali, Burkina Faso, and northern Nigeria. The associated MCSs are typically not locally generated, forming instead at distances greater than 100 km upstream. Composites reveal that a significant increase in atmospheric moisture content occurs prior to development, but there is no evidence of significant changes in the 600 – 925 hPa vertical wind shear. This indicates that changes in vertical wind shear are less influential in extreme storm development than atmospheric moisture preconditioning.

The top 10 events are further evaluated. A change in these storms' direction and speed near the maximum rainfall location is common, suggesting the MCSs are reorganizing around peak rainfall intensity time. Three atmospheric conditions are associated with these events. They are (1) moisture preconditioning of the atmosphere, (2) interaction of the storm in the wake of a region of anticyclonic flow, and (3) interaction of the storm in the wake of a region of anticyclonic flow and the Sahel/tropical dryline boundary.

Keywords: West African Sahel, extreme rainfall, mesoscale convective system (MCS), African easterly wave, intertropical front, intertropical discontinuity, dryline, vertical wind shear, flooding

Declarations:

Funding: This work was funded by NSF Award #1929074

Conflict of interest: Not applicable

Availability of data: All datasets analyzed in this study are freely available from their original sources.

50 Code availability: Not applicable

1. Introduction

Heavy rainfall events are a major weather hazard over the semi-arid Sahel and Soudan of West Africa. During the boreal summer, such events frequently occur when strong organized areas of convection such as mesoscale convective systems (MCSs) and West African squall lines move across sub-Saharan Northern Africa. These systems can deliver copious rainfall in often short periods resulting in flooding that impacts the health and livelihoods of the population (Tschakert et al. 2010; Anash et al. 2020). Given the likelihood that such heavy rainfall events may become more frequent and/or intense in the future (Han et al. 2019; Kendon et al. 2019; Fitzpatrick et al. 2020), and observations that suggest this intensification is underway (Taylor et al. 2017; Tramblay et al. 2020; Klein et al. 2021), there is a crucial need to better understand how these rainfall systems develop in order to improve our climate-scale predictive capabilities.

The purpose of this study is to identify rainfall systems that produce heavy rainfall events over the West African Sahel/Soudan, understand where these events occur including where the associated MCSs originate, and assess the relative importance of environmental conditions including the preconditioning of moisture in the atmosphere and the vertical wind shear on storm development. Doing so will enhance our fundamental understanding about how intense rainfall events form, as well as improve our current and future predictive capabilities by pointing to the environmental factors that are most relevant.

Background is provided in Section 2. Section 3 describes the datasets and analysis methods utilized. Results are presented in Section 4, while findings are summarized and conclusions drawn in Section 5.

2. Background

Advancing our understanding of extreme rainfall events over the West African Sahel/Soudan requires a basic understanding of how rainfall is delivered, particularly during the boreal summer monsoon season when most of the rainfall occurs. It is estimated that between 70 – 95% of the total rainfall over this region is associated with organized convective systems (Laurent et al. 1998; Laing et al. 1999; Mathon et

al. 2002; Mohr 2004; Liu et al. 2019) including bowing squall lines (Eldridge 1957; Desbois et al. 1988; Peters and Tetzlaff 1988; Rowell and Milford 1993; Fink and Reiner 2003) as well as other types of organized MCSs (Laing and Fritsch 1993; Laurent et al. 1998).

Heavy rainfall events and associated flooding due to inundation and runoff are acute problems throughout the world. This includes West Africa and the Sahel/Soudan where extreme rainfall events lead to storm-related damage to homes/property, economic hardships due to crop and livestock losses, displacement of the population from flood-prone areas, and flood-related fatalities (Di-Baldassarre et al. 2010; Panthou et al. 2014).

Storms that deliver copious amounts of rainfall often develop quickly, providing minimal lead time to warn the population and prepare for adverse consequences (Engel et al. 2017). Flooding potential is exacerbated over urban areas where the density of buildings, roads, and pavement enhances runoff in areas where there are high population densities (Douglas et al. 2008). Since the 1980s, the frequency of these stronger, better organized rainfall producing storm systems over the West African Sahel has changed (Taylor et al. 2017), accompanied by an observed increase in storm intensity and flood damage (Giorgi et al. 2011; Panthou et al. 2014). Climate model projections (Kundzewicz et al. 2014; Han et al. 2019; Kendon et al. 2019; Fitzpatrick et al. 2020) indicate that these types of events are likely to become more frequent and/or intense under global warming. These changes in rainfall will undoubtedly lead to an increase in flood-related property damage and deaths over the West African Sahel/Soudan, amplified by growing populations (Panthou et al. 2014).

Environmental factors influence the development and lifespan MCSs. Most favorable for development is a moist, conditionally unstable environment with a lifting mechanism to trigger deep convection (Doswell et al. 1996). Specific to the West African Sahel/Soudan, the low-level inflow of moist, tropical flow from the Gulf of Guinea (Cook 1997; Hagos and Zhang 2010; Thorncroft et al. 2011; Cook 2015; Vizy and Cook 2018) and the development of African easterly waves (AEWs; Carlson 1969a, b; Burpee 1972; Reed et al. 1977) are conducive to development. There are two preferred storm tracks across sub-Saharan northern Africa, namely a southerly track between 8°N - 15°N, and a northerly track north of

15°N (Diedhiou et al. 1999; Fink and Reiner 2003; Hsieh and Cook 2005, 2008; Mekonnen et al. 2006). In the southern storm track, MCS activity tends to occur to the west of the AEW trough (Burpee 1972; Tetzlaff and Peters 1988), while in the northern storm track convection tends to occur to the to the east of the trough where there is enhanced southerly flow of moist air (Burpee 1972; Duvel 1990; Mathon et al. 2002; Fink and Reiner 2003). AEW disturbances perturb the mid-tropospheric horizontal shear associated with the mid-tropospheric African easterly jet (AEJ) as well as the vertical wind shear, both of which can be important factors for the development squall lines and MCSs (Rowell and Milford 1993; Hodges and Thorncroft 1997; Mohr and Thorncroft 2006). In particular, shear plays a crucial role in organizing convection into MCSs (Barnes and Sieckman 1984; Rotunno et al. 1988; Weisman and Rotunno 2004).

Topography is also influential in storm development and organization over the West African Sahel/Soudan. Elevated terrain promotes vertical lifting of the low-level flow, and differential surface heating generates near surface convergence boundaries that can help convective systems develop and organize during the daytime (Tetzlaff and Peters 1988; Mohr and Thorncroft 2006; Laing et al. 2008; Vondou 2012). MCSs are observed to propagate away from elevated terrain during the evening/night, bringing heavy rainfall to areas downstream away from the topographic feature (Mohr 2004; Zhang et al. 2016a, b; Vizy and Cook 2018, 2019a). This suggests that the diurnal cycle plays a pivotal role in storm formation and development over West Africa (Parker et al. 2005).

Smaller scale processes, such as surface moisture gradients, and cold pool outflow/air mass boundaries also influence MCS development over West Africa. Variations in land surface moisture due to rainfall, and/or the proximity of wetlands or lakes can influence the development of convection, with afternoon convection more likely to occur over a drier surface (Taylor 2010, Taylor et al. 2012, 2013; Taylor et al. 2018). Mechanistically, sensible heating is enhanced over the drier surface which can help form strong low-level temperature gradients that can perturb the low-level circulation and generate convergence boundaries with strong vertical ascent favorable for the development of convection, especially when in relatively close proximity to a wetter surface. Cold pool outflow boundaries are formed when evaporative cooling of falling precipitation within an MCS results in a downdraft of relatively cool air that

expands radially near the surface. A mesohigh is formed, with strong gust fronts that become convergence boundaries, along which additional convective cells can develop (Zipser 1977; Redelsperger and Lafore 1988; Marsham et al. 2013; Dione et al. 2014; Provod et al. 2016). Airmass boundaries form between the moist, tropical West African monsoon air and dry, Sahel/Saharan air across West African Sahel during the boreal summer. The moist air is shallow near the frontal boundary, deepens equatorward, and varies over the diurnal cycle (Parker et al. 2005). These frontal zones provide a capping inversion for low-level turbulence that delays the release of convective instability (Carlson et al. 1983; Trier et al. 2004, 2015). This allows for the build-up of stronger instability and the development of stronger MCSs over the Sahel (Vizy and Cook 2018, 2019a), operating in a manner similar to that of a dryline frontal boundary (Eldridge 1957). In the existing literature (e.g., Hamilton and Archbold 1945; Hastenrath and Lamb 1977; Lélé and Lamb 2010) this frontal boundary over West Africa is often referred to as the Intertropical front (ITF) or Intertropical discontinuity (ITD), but these names are not accurate since an intertropical front is technically defined as a front within the equatorial trough that separates the air of the Northern and Southern Hemisphere (American Meteorological Society 2021), and the West African Sahel/Soudan lies well north (12° - 20° of latitude) of the equator. To avoid confusion, we refer to this airmass boundary as the Sahel/tropical Africa dryline boundary.

While these factors play an important role in the development of convection over the region, it is less clear why some storms are more extreme than others. Progress on this issue has been limited over West Africa as most studies focus on individual events and/or particular regions (Tarhule 2005; Samimi et al. 2012; Magami et al. 2014; Panthou et al. 2014; Zahiri et al. 2016; Anash et al. 2020). For example, Knippertz and Martin (2005) evaluated 3 cold season extreme rainfall events over West Africa and found that tropical-extratropical interactions led to a plume of moisture over West Africa that plays an important role in development. Engel et al. (2017) examined two high-impact heavy rainfall events over urban areas, namely, Ouagadougou on 1 September 2009 and Dakar on 26 August 2012. Unusual synoptic-convective dynamic developments led to the exceptional rainfall totals for both events. The Ouagadougou event was

associated with AEW breaking (Galvin 2010; Cornforth et al. 2017) that resulted in two strong MCSs passing over the city within 6 hours.

Schlueter et al. (2019a, b) develop a broader understanding of storm systems over the region by evaluating the relationship between rainfall and six wave types over sub-Saharan northern Africa. The six types are eastward intertial-gravity waves, AEWs/tropical disturbances, Kelvin waves, mixed Rossby-gravity waves, equatorial Rossby waves, and Madden-Julian oscillation (MJO) waves, and they operate on timescales ranging from sub-diurnal to intraseasonal timescales. The constructive and destructive interactions among the waves offer some promise in explaining the development of extreme convective events over West Africa. Slower moving waves such as the MJO and equatorial Rossby waves primarily impact summer monsoon dynamics, while faster AEWs, Kelvin waves, and mixed-Rossby gravity waves primarily modulate moisture convergence and have a more direct effect on precipitable water over West Africa and the Sahel. This is consistent with prior studies (Matthews 2004; Janicot et al. 2009, 2011; Leroux and Hall 2009; Alaka Jr and Maloney 2012, 2014) that indicate the MJO can have a significant remote influence on convection over West Africa during boreal summer.

There is a need to further improve our fundamental understanding of the development of extreme rainfall events over the West African Sahel/Soudan. In this study we contribute by examining the development of the systems that deliver the heaviest 24-h rainfall total over a broad region of the West African Sahel.

3. Datasets and Methodology

3.1 Datasets

High spatial resolution datasets at timescales most relevant for storm development (e.g., 1 hour or less) are needed to identify heavy rainfall events and understand the environmental conditions associated with their development. For rainfall, we utilize the NASA Long-term Integrated Multi-satellitE Retrievals for global precipitation measurement Version 06B final run (IMERG; Hou et al. 2014; Huffman et al. 2020). This 0.10° resolution product yields rainfall estimates globally by fusing measurements from the Global

Precipitation Measurement (GPM) satellites (2014 – present) with estimates from the Tropical Rainfall Measuring Mission (TRMM) satellites (2000 – 2014). IMERG provides 30-minute rainfall estimates over the past 20 years which is sufficient for identifying extreme rainfall events. While IMERG provides a variety of rainfall estimates, we use the calibrated final-run rainfall product for this study because it is thought to provide a reasonable estimate (Dezfuli et al. 2017; Maranan et al. 2020; Tapiador et al. 2020), and is generally found to be more accurate than IMERG early-run and late-run products (Wang et al. 2017; Omranian and Sharif 2018; Mahmoud et al. 2018; Li et al. 2021).

181

182

183

184

185

186

187

188

189

190

191

192

193

194

195

196

197

198

199

200

201

202

203

204

205

206

Additional data sources are examined to ground-truth heavy rainfall events identified from IMERG. This is necessary because there is uncertainty in estimating rainfall from satellite measurements as processing algorithms make assumptions regarding a variety of issues such as temperature profiles and droplet sizes, and filling in for limited spatio-temporal coverage can affect the final rainfall estimate (Kidd and Levizzani 2011; Pfeifroth et al. 2013, 2016). For regions with reliable and comprehensive rain-gauge networks, the most effective method of validation is to cross-reference satellite precipitation estimates with available ground truth gauge measurements (Nair et al. 2009; Gaona et al. 2016; Watters et al. 2018). This is a less viable option over the West African Sahel, where ground-based measurement networks are more limited (Nicholson et al. 2003; Roca et al. 2010; Dezfuli et al. 2017; Maranan et al. 2020). To provide some level of ground-truth confirmation and validation of IMERG, events identified in IMERG are crossreferenced with impact-driven information from the Centre for Research on Epidemiology of Disasters (CRED) Emergency Events database (EM-DAT; EM-DAT 2020), the Famine Early Warning Systems Network (FEWS NET) weekly weather hazards for Africa summaries (FEWS NET 2020), the United Nations Office for the Coordination of Humanitarian Affairs (OCHA) Reliefweb reports, International Federation of Red Cross and Red Crescent Societies Disaster Relief Emergency Fund (DREF) bulletins, and independent published articles.

The ECMWF ERA5 reanalysis (ERA5, C3S 2017) is analyzed to relate the heavy rainfall events to the larger-scale environmental conditions. ERA5 is a 5th generation product that provides global 0.25° resolution hourly gridded output of atmospheric and surface fields from 1979 – present. The finer spatial

and temporal resolutions of ERA5 make it a reasonable data source to understand environmental conditions at sub-diurnal timescales (Danso et al. 2019; Vizy and Cook 2019b; Li et al. 2020).

3.2 Methodology

IMERG rainfall estimates are used to identify the wettest 24-h rainfall events over the West African Sahel between 2000 – 2019. Here, the West African Sahel is defined as the area from 8.05°W – 12.95°E and 12.05°N – 17.95°N, as shown in Fig. 1. These bounds are set to avoid prominent terrain features including the Jos Plateau of Nigeria to the south (9°N; 9°E), the Guinean Highlands (8°N; 10°W) to the southwest, the Aïr Mountains of Niger to the north (18°N; 9°E), and Lake Chad to the east (13°N; 14°E).

While some heavy rainfall events last for multiple days and are associated with several rounds of convective activity, our focus is on shorter, sub-diurnal rainfall events associated with the development of MCSs. This includes African squall lines which are known to frequently occur during the boreal summer. This means that the temporal and spatial continuity of the rainfall area is important to the event definition to distinguish it from extreme rainfall that may be produced by a series of events. We apply a 12Z – 12Z 24-h window and use it to identify the dates and location of the largest 24-h rainfall events in the region. The 12Z – 12Z time window aligns with our the typical MCS lifecycle over the Sahel. In many, but certainly not all, instances over the West African Sahel/Soudan, MCSs are more likely to develop in the afternoon shortly after peak daytime heating, often persisting and in some instances intensifying during the evening/night hours before weakening the following morning (Fink et al. 2006; Laing et al. 2008; Zhang et al. 2016a; Vizy and Cook 2019a). Our results may have some dependence on this time window.

To determine the events that produce the top 100 wettest 24-h rainfall totals, we calculate the 12Z – 12Z accumulated total rainfall for every day from 2000 – 2019 for each IMERG grid point in the defined analysis region. The grid point totals are then ranked from highest to lowest to find the top 100 wettest independent events. To identify independent events, a grid point under consideration cannot be associated with a rainfall event that has already been identified as having a higher 24-h rainfall total on the same day within 500 km distance of this location. This criterion is necessary because heavy rainfall events are likely

to impact a spatial area greater than the size of a single grid point. Thus, the top 100 events are identified by their location and date, and as it turns out each event occurs on a different date from the other top 100 events.

233

234

235

236

237

238

239

240

241

242

243

244

245

246

247

248

249

250

251

252

253

254

255

256

257

258

The top 100 events are analyzed to evaluate where the extreme rainfall events occur based on the maximum 12Z - 12Z 24-h total precipitation location and where the MCS primarily responsible for the extreme event originated. The top 100 cases are examined out of convenience, as it is a manageable number of events to work with, yet it provides a large enough sample to understand differences among the extreme events. The monthly occurrence distribution and the area of the daily total accumulated precipitation associated with each event for various rainfall thresholds is quantified. Compositing is used to evaluate changes in important environmental conditions for storm development including precipitable water and vertical wind shear. Composites are formed by averaging the desired field over the 100 events at the same time of day in the diurnal cycle, and composite anomalies are calculated by subtracting the top 100 composite from a weighted climatological mean value determined by the months for which the events occur. Weighting is necessary because the top 100 events occur with different frequency over the boreal warm season of May – October. Event frequency closely follows the seasonal evolution of the West African summer monsoon system rainfall over the Sahel with peak rainfall activity in August, and rainfall tailing off in the months adjacent to August (Cook 1997, 2015). Here, climatological monthly mean values are assigned a weight of 1/100 May, 3/100 June, 24/100 July, 59/100 August, 9/100 September, and 4/100 October, and added together to obtain the weighted climatological value.

To evaluate storm trajectories and the sizes of the rainfall shield and the convective core for the top 10 events, we have adapted the approach of Vizy and Cook (2018, 2019a) to track MCSs. A threshold rainfall rate of 100 mm day⁻¹ is used to defined the storm's rain shield at any given time. This rainfall rate threshold is selected to provide an estimate for the more intense convective core of the system where the largest percentage of the rainfall is likely to fall from for the event. Following Vizy and Cook (2018, 2019a), we assume that the convective core rain shield is at least 2000 km² in size, in this case 16 or more contiguous grid points meeting the threshold rainfall rate value. The centroid of the above-defined rain

shield is determined to define the storm's location at a given time. Then starting at the time of the peak rainfall intensity, the storm is objectively tracked forward and backward in time until either the 100 mm day⁻¹ rainfall shield no longer meets the 2000 km² size criterion, or the storm can no longer be tracked due to merging or splitting of the storm's convective core rain shield. Additionally, the size of the storm areal extent is also evaluated for the identified storm throughout its development. This involves evaluating the size of the 5 mm day⁻¹ and the 500 mm day⁻¹ rainfall shields with the former threshold selected to represent the entire system including areas associated with stratiform rainfall, while the latter threshold selected to represent the most intense convective core of the system. Finally, relevant atmospheric conditions from ERA5 are examined for select cases.

4. Results

4.1 Events with the highest rainfall totals: The top 100

Figure 1a shows the location of the top 100 12Z – 12Z 24-h maximum rainfall rate events for the analysis region, while Table 1 provides information for each event. Top 100 events occur infrequently over the northern Sahel within the analysis region, with the vast majority occurring south of 14°N over the Soudan. There are 3 regions where events cluster over the southern Sahel/Soudan. They are over southwestern Mali (~11°N, 8°W; 24 events), central Burkina Faso (~13°N, 2°W; 10 events), and north-central Nigeria (~12°N, 8°E; 17 events). Each of these regions has a strong connection with topography. Most events over Mali occur on the eastern slopes of the Mandingue Plateau (~13°N, 9°W), over Burkina Faso in close proximity to the North Mossi Plateau (~13°N, 2.5°W), and over north-central Nigeria to the northern slopes of the Jos Plateau (~12°N, 9°E). Elevation changes associated with these topographic features are modest, usually only 200 – 400 meters, compared to other regional features such as the Aïr Mountains of northern Niger (18°N, 9°E) and the Cameroon Highlands (6°N, 11°E). However, they are apparently large enough to provide the necessary dynamical forcing of moisture eddies that can help the development of heavy rainfall amounts when the synoptic environment is favorable. For the 9 most intense events, with rainfall totals greater than 200 mm, 8 occur south of 14°N. The one event north of 14°N

occurred southeast of the Aïr Mountains of north-central Niger in the Damergou Gap, and it is the highest maximum total 24-h event identified in this study.

The MCSs associated with the top 100 rainfall events are back-tracked to find their genesis locations, shown in Fig. 1b. 94% originate between 10°N and 20°N. The longitudinal distribution is more uniform, with 29 generated west of 0°E, 35 between 0°E - 10°E, 17 between 10°E - 15°E, and 19 east of 15°E primarily over central and southern Chad and the Darfur Mountains of the Sudan. Thus, the distance between the genesis region and the location of maximum rainfall (Fig. 1a) can be large. Only 25 of the 100 events form locally, defined here as when storm genesis occurs within 100 km of the maximum 24-h rainfall location. Of the other 75 events, 44 form between 100 – 1000 km away from the maximum rainfall location, 24 form 1000 – 2000 km away, and 7 form over 2000 km away.

While topography is known to be associated with MCS generation, less than half of the 100 selected storms originate over larger orographic features, including the Ahaggar Mountains of southern Algeria (3 storms), the Aïr Mountains of Niger (7 storms), and the Marra Mountains in the Darfur region of Sudan (8 storms). For the other cases, many of these MCSs originate with help from elevated terrain relative to the surroundings, and/or in proximity to areas with wetter surfaces and/or a moisture gradient exists. The most active storm genesis location is in the Lake Chad depression where 15 of the top 100 events originate (Fig. 1b). Whether and how Lake Chad contributes to storm development is under investigation in a separate study (Zhao et al. 2022).

In regards to the three event cluster regions mentioned earlier, for the 24 Mali event genesis locations, 5 form locally within 100 km of the maximum location, 10 form to the east over Burkina Faso, while the remaining 9 form more remotely at distances greater than 900 km from the Mandingue Plateau of Mali. For the Burkina Faso events over the North Mossi Plateau, 1 event forms locally while 3 originate to the north and east over the Ahaggar (~23°N, 6°E) and Aïr (~18°N, 9°E) Mountains. The remaining 6 events have origins east of Burkina Faso, primarily over the Jos Plateau region of Nigeria. For the north-central Nigeria events, 3 form locally, while 3 form east of 20°E. Most of the MCSs associated with extreme rainfall events over this region (11 events) originate in the vicinity of Lake Chad (~13°N, 12°E).

Table 1 also provides information on the duration and maximum rainfall intensity of each event. Seven of the longer events, that is, events that exceed 1 standard deviation over the mean, are among the 25 events with highest rainfall, with 4 in the top 10. In contrast, only 2 of the shorter duration events are among the top 25, and none are among the top 10. For peak rainfall intensity, 6 of the highest maximum intensity events are in the top 25, including 3 among the top 10. Conversely, only 2 of the lower peak intensity are in the top 25, and both are long duration events.

Figure 2a shows how rainfall totals are distributed for the top 100 events listed in Table 1. The wettest has a maximum of 291 mm with totals decreasing exponentially, falling below 200 mm by event 10, 175 mm by event 26, and 150 mm by event 78. It is 7.5 times more likely to have a maximum rainfall total between 150 - 200 mm than greater than 200 mm.

Figure 2b displays the seasonality of the top 100 events along with the area-averaged climatological monthly IMERG precipitation for the analysis region box. 83 of the 100 events occur during the peak of the summer monsoon season, with 24 in July and 59 in August. There are only a few events in May, June, September, and October, and none from November to April. The occurrence frequency is consistent with the seasonal cycle of rainfall over the analysis region, as both peak in August. Furthermore, the vast majority of these events occur south of 14°N, which is just south of the climatological summertime locations of the surface baroclinic zone and the mid-tropospheric AEJ.

Figure 3 shows the 24-h areal size of the top 100 events for various rainfall total thresholds. The bars are color coded to indicate event rainfall totals at 25 mm intervals from 100 mm – 200 mm. The majority of the top 100 events deliver 24-h rainfall totals exceeding 100 mm over an area of around 4000 km² or less. The heavy-rain (>100 mm) areas of 12 of the top 100 events are greater than 20,000 km², with 6 of these events ranked in the top 10 (Table 1). This indicates that the highest 24-h precipitation totals, that is, the events that lie on the steepest part of the distribution curve shown in Fig. 2a, are more likely to have a larger areal coverage.

Composites formed from the top 100 events are compared with climatological conditions to better understand the environmental conditions associated with these extreme cases. Fig. 4a shows the

climatological precipitable water and low-level 925 hPa winds at 12Z, while Fig.4b shows the composite anomalies. Climatologically, precipitable water is greater than 45 mm south of 14°N, indicative of the deep moist tropical air that is typically transported into West Africa via the low-level southwesterly monsoon flow during the boreal summer. North of 14°N precipitable water decreases to about 30 mm by 20°N, reflective of the increasingly shallow depth of the monsoon. Most of the extreme events (Fig. 1a) occur where the climatological precipitable water is greater than 40 mm. Note, from a climatological perspective, most of the moisture in the atmospheric column is found at low-levels, typically below 800 hPa.

Extreme events are associated with a significant and widespread increase in precipitable water over the entire Sahel/Soudan (Fig. 4b). In the analysis region, precipitable water is greater by 1-3 mm (4-9% increase) during these events, and even more so over the northern Chad Bodélé (> 4 mm or a 10-14% increase) upstream of the analysis region. The increase over Chad is associated with a significant increase in the low-level southwesterly flow into the Bodélé. There is also a significant change in the low-level flow in the analysis region over Burkina Faso. Here the anomalous low-level flow is primarily zonal, indicating a more westerly low-level monsoon flow over Burkina Faso and from Ghana to Nigeria.

Fig. 4c shows the climatological 12Z wind difference between 600 – 925 hPa. There is strong zonal vertical wind shear over the West African Sahel with magnitudes greater than 14 m s⁻¹ extending from the Senegal coast eastward to Chad. The anomalies at 12Z (Fig. 4d) indicate that, outside of a few isolated areas including the Bodélé of Chad and Côte d'Ivoire, pronounced differences in vertical wind shear are not associated with extreme rainfall totals in the composite. This result is independent of the compositing hour selected, as the 12Z anomaly pattern in Fig. 4d is consistent with those at other hours (not shown). Examination of the individual events comprising the composite indicates that the wind shear strength is anomalously weak compared to the climatology in 46 events and anomalously strong in 54 events in the 3 hours prior to the peak rainfall rate at the maximum site. (see last column of Table 1). If composites are formed individually using only events from one cluster area, namely, the Mali, Burkina Faso, and Nigeria region clusters, the conclusion is the same. It should be noted that the analysis region

has relatively strong climatological vertical shear to start (Fig. 4c), so vertical shear may still be strong enough to make mesoscale organization possible even when vertical shear is anomalously weaker.

We conclude that extreme rainfall events in the analysis region are associated with a robust and significant increase in the atmospheric moisture content, not only over the region but over the entire Sahel. We do not find a connection to vertical wind shear.

4.2 Events with the most extreme rainfall totals: The top 10

Fig. 2a indicates a clear inflection point in the rainfall distribution curve at event 10. In this section we examine these top 10 events that deliver the highest rainfall totals (see Table 1) to gain a better understanding about the development of these storms, and extreme storms in general over the West African Sahel/Soudan. Figure 5 shows the distribution of 24-h accumulated precipitation greater than 50 mm for each of these events. The red circles denote the location of the maximum rainfall for each case. There is no obvious similarity among the events, and they range from localized events (CASE01 and CASE08) to widespread events (CASE02 and CASE06).

Figure 5 also speaks to the potential impact of each event, especially in terms of flooding potential due to the total amount of accumulated precipitation over the 24-h period. For example, CASE01 which is associated with the highest maximum 24-h rainfall total (Table 1), has a limited area of heavy rain over central Niger with a more widespread area of 50 – 100 mm of rainfall extending from central Niger into northern Nigeria. Thus, it could be inferred from Fig. 5a that flash flooding for this case would be more likely localized over central Niger. In contrast, CASE02 and CASE07 are associated with widespread 24-h rainfall totals exceeding 150 mm over the Niger River basin in southern Mali that likely not only impact communities and cities including Bamako immediately after the event, but also the downstream Niger River communities in the days that follow.

FEWSNET reports, CRED EM-DAT disaster reports, OCHA Reliefweb, and DREF bulletin reports along with any available extreme rainfall studies are examined to attempt to confirm via ground-truth the impacts of the top 10 events. Results are summarized in Table 2, and indicate that 5 of the events

(CASE01, CASE03, CASE04, CASE06, and CASE08) are directly associated with impactful flooding. For CASE02, CASE05, CASE07, and CASE09, available reports are vague on the exact timing of the flooding, and/or reports suggest that multiple events over many days led to the flooding. For CASE10, no ground-truth evidence is found, so it is unclear how impactful it is. Overall, the ground-truth results are encouraging, and give us confidence that we have identified impactful rainfall events.

Fig. 6 shows the diurnal time series of rainfall for the maximum 24-h total precipitation location (the red circles in Fig. 5) for the top 10 events. The gray lines in each panel denote the time of the maximum rainfall rate intensity for each event. Event types range from relatively shorter duration/higher peak rainfall intensity cases such as CASE01, CASE04, CASE08, and CASE10, to longer duration/weaker peak rainfall intensity cases such as CASE02, CASE03, CASE06, and CASE09. Longer duration/weaker peak intensity events occur primarily after 00Z, while the shorter duration/higher peak intensity events tend to occur in the late afternoon and evening.

To put into context how representative the above findings are for the larger population, all 100 events are also categorized by diurnal cycle. We calculate the mean and standard deviation for event duration and event peak intensity (Table 1), then select cases in which both the duration and peak intensity fall outside the \pm 0.5 standard deviation level. This yields a list of events for the two diurnal types as well as the opposite categories, namely the longer duration/higher peak intensity and shorter duration/ weaker peak intensity events (Table 3). We find that there are 14 longer duration/weaker peak intensity and 14 shorter duration/ higher peak intensity events out of the top 100 cases. These types are approximately 3 times more likely to occur than the longer duration/higher peak intensity and shorter duration/weaker peak intensity types. Furthermore, the selected longer duration/weaker peak intensity events yield a larger 100 mm rain shield area (Fig. 3) and 7 are associated with an area greater than 10,000 km² compared to 1 event at this size for the shorter duration/higher peak intensity type.

Fig. 7a shows the diurnal cycles of rainfall for the 14 longer duration/weaker peak intensity events (gray lines) listed in Table 3 along with the composite means (red line), while Fig. 7b shows their locations. While rainfall occurs prior to 00Z in some events, there is a clear preference for peak rainfall rates between

00Z to 03Z. 11 events (78%) occur over Burkina Faso and Mali and the remaining 3 events occur north of the Jos Plateau of Nigeria.

Fig. 7c shows the diurnal cycle of rainfall for the 14 shorter duration/higher peak intensity cases. The time of peak rainfall intensity is more variable for this type, so the composite mean is relatively constant over the diurnal cycle. Event locations (Fig. 7d) are evenly distributed longitudinally, with 6 cases east of 2°E and 8 cases west of 2°E. There is no clear association between the timing of peak rainfall intensity and the location for these events.

In summary, this analysis confirms that the top 10 events are representative of the larger, top 100 population. That is to say the top 10 population does not consist of just one type of event. Instead, it includes storms across a spectrum ranging from longer duration/weaker peak intensity to shorter duration/higher peak intensity events that are also shown to occur in the larger population (Fig. 7). This gives us confidence that the results focused on the top 10 events are applicable not only to the individual storms being analyzed, but also to a more robust population of storms.

Figure 8 shows the trajectories of the convective cores for the 10 events prior to (green) and following (blue) the time of peak rainfall intensity. As mentioned in section 3 the convective core is defined using a relatively high rainfall rate threshold (100 mm day⁻¹). Rain shields of this magnitude vary in duration among the cases, so some trajectories in Fig. 8 have more points than other events. For example, CASE03 (Fig. 8c), CASE06 (Fig. 8f), and CASE09 (Fig. 8i) have relatively few tracking points and they tend to be spaced closer together indicating a shorter lived and slower moving convective core for these longer duration/ weaker peak intensity events. For CASE01 (Fig. 8a), CASE04 (Fig. 8d), and CASE10 (Fig. 8j) there are more tracking points covering a larger area, indicating the strong convective core is longer lasting and, in most cases, faster moving for the shorter duration/ higher peak intensity events. However, not all events conform to this characterization. For example, CASE02 is a long duration/weak peak intensity type, but the convective core is relatively long lasting and covers a large area. Likewise, CASE08 is a short duration/high peak intensity type, but the convective core is shorter lived as the storm is more limited in size compared to other top 10 events (Fig. 3).

Fig. 8 indicates that some storms change direction when the storm is in close proximity to the location of maximum rainfall rate (red circle). Examples include CASE01 (southwesterly to a southwesterly track shift), CASE05 (west-southwesterly to a southwesterly track shift), and CASE10 (west-southwesterly to a south-southwesterly track shift). The physical processes responsible for directional change could be influential in producing heavy rainfall totals for some events, for example, through a reorganization in the convection in response to environmental condition changes. Future work can explore this possibility and the implications for storm intensification.

One way to understand how a storm reorganizes over time is to examine how the physical size of the storm and the size of the convective core change. Fig. 9 shows the timing of the storm rain shield area development for each case. Two areas are shown. One, denoted by the black line, is the size of the rain shield defined by the 5 mm day⁻¹ rainfall rate threshold for the MCS that passes directly over the maximum site location. This represents an estimate of the area of the entire MCS that includes the convective and stratiform components of the system. The other area, indicated by the blue line, is an estimate of the intense convective core that passes over the maximum site location. It is defined by the 500 mm day⁻¹ rainfall rate threshold. Thus, if a passing MCS consists of multiple intense convective cores that are not continuous at the defined threshold level, only the core(s) that directly pass over the maximum site location are accounted for in the areal estimate. The gray line denotes the time of peak rainfall rate at the storm's most intense location.

Fig. 9 indicates that events range in size from generally less than 200,000 km² (CASE03, CASE08, and CASE09), to mid-size between 200,000 – 400,000 km² (CASE01, CASE04, CASE05, and CASE10), to greater than 400,000 km² (CASE02, CASE06, and CASE07). No apparent relationship is found between the areal size of the MCS rain shield and the longer duration/weaker peak intensity events as two cases are relatively large in size (CASE02 and CASE06), and two events are small in size (CASE03 and CASE09). In contrast, 3 of the 4 shorter duration/higher peak intensity events are mid-sized (CASE01, CASE04, and CASE10), while the fourth case, CASE07, eventually exceeds 400,000 km².

The convective cores range in size from less than 10,000 km² for CASE01, CASE03, CASE08, CASE09, and CASE10, to over 20,000 km² for CASE02, CASE04, CASE05, and CASE06. When peak rainfall intensity occurs, there is a relative peak in the size of the convective core for most cases. This indicates that the convective core grows in size around the time of peak intensity. In most instances, when the intense convective core size is growing, the MCS temporarily contracts in size. In some cases, such as CASE01 (Fig. 10a), CASE02 (Fig. 10b), and CASE06 (Fig. 10f), this happens multiple times over the storm's lifespan, signifying a potential cycle of convective core growth and decay that is generally opposite that of the larger MCS system. Furthermore, the most intense rainfall rate does not necessarily correspond to when the convective core size is largest. It is unclear if this is a physical change in the storm development, or an artifact of the blending of different types of satellite data in IMERG (Rajagopal et al. 2021).

4.3 Environmental conditions associated with the top 10 heavy rainfall events

While a variety of environmental factors may be associated with extreme rainfall development, three conditions are identified here as being particularly important. Each is discussed below.

4.3.1 Moisture preconditioning of the atmosphere

Figure 10a shows ERA5 700 hPa geopotential height, 700 hPa wind, and precipitable water anomalies, while Fig. 10b shows the anomalous vertical wind shear for CASE01 for a representative time prior to the peak rainfall intensity. A strong mid-level disturbance was positioned east of the maximum rainfall location along the Niger/Chad border prior to the rainfall maximum for this short duration/ high peak intensity event. Anomalous cyclonic flow enhances atmospheric moisture loading over the central Sahel in support of the high rainfall totals over eastern Niger. There is a concentrated core of anomalously high meridional vertical shear in the vicinity of the site exceeding 12 m s⁻¹ associated with the flow around the disturbance. South of 15°N there is a broad region of anomalously weak zonal shear associated with a weakening of the mid-level easterly flow.

CASE03 (Fig. 10c & d) and CASE06 (Fig. 10e & f) are also associated with strong moisture loading over much of the Sahel. Both are long duration/weak peak intensity events. Comparable to CASE01, the precipitable water values are 15 – 25 mm higher than average between 15°N - 22°N for CASE06 (Fig. 10e), and 5 – 10 mm higher for CASE03 (Fig 10c). Both of these cases have strong disturbances in the southern AEW storm track that are associated with anomalous westerly/west-southwesterly flow. The Sahel/tropical Africa dryline boundary is positioned north of 20°N for both cases, consistent with CASE01, indicative of a relatively deep layer of moisture across the Sahel for all three cases. CASE03 (Fig. 10d) is associated with a strong negative anomaly in the vertical zonal wind shear, while CASE06 (Fig. 10f) is located at the boundary between anomalously strong meridional vertical shear to the west and anomalously weak zonal vertical shear to the east.

Hovmöller plots of the 700 hPa relative vorticity and precipitable water anomalies averaged between 10°N - 15°N for the 3 cases are shown in Fig. 11. The circles in each panel denote the longitudinal position and time of the peak rainfall intensity at the maximum rainfall site. Propagation speeds estimated from the 700 hPa relative vorticity plots for relevant disturbances are noted.

CASE01 (Fig. 11a) is associated with a relatively slow-moving disturbance (5.5 m s⁻¹) that is trailing a faster moving disturbance (9.5 m s⁻¹). While the anomalous precipitable water (Fig. 11b) is primarily high in the 10-day window shown, the first disturbance is influential in further enhancing the atmospheric moisture. CASE03 (Fig. 11c) occurs in a particularly active period with multiple disturbances propagating across the Sahel. Like CASE01, the environment for CASE03 is anomalously moist west of 10°E over the 10-day period shown (Fig. 11d). The disturbance most closely associated with the event originates around 15°E and propagates at a speed of 7.4 m s⁻¹ to about 4°W, then it slows to 4.6 m s⁻¹. The peak intensity of rainfall coincides with this slowdown. CASE06 (Fig. 11e) is associated with two relatively strong disturbances with the first moving faster than the second, helping to further enhance the atmospheric moisture over West Africa prior to the second system (Fig. 11f). The event is closely associated with the second disturbance which is relatively slow moving (5.5 m s⁻¹).

Overall, the three events are associated with an unusually large build-up in the atmospheric moisture content over the Sahel over the days prior to the event. Accompanying this moisture build-up is a poleward retreat north of 20°N of the Sahel/tropical Africa dryline boundary. This moisture-laden environment is conducive for heavy rainfall, which occurs when approaching disturbances along the southern AEW storm track move over the region.

4.3.2 Interaction of the storm in the wake of a region of anticyclonic flow

Fig. 12 shows ERA5 700 hPa geopotential height, wind, precipitable water, and vertical wind shear anomalies for select times of the CASE02 (Fig. 12a & b), CASE07 (Fig. 12c & d), and CASE10 (Fig. 12e & f) events. CASE02 (Fig. 12a) and CASE07 (Fig. 12c) are associated with strong disturbances in the southern AEW storm track. Flow is anticyclonic ahead of the approaching disturbance, associated with anomalously drier conditions over Senegal, Guinea, southwestern Mali, Sierra Leone, Liberia, and Côte d'Ivoire. Vertical wind shear is enhanced for both cases (Figs. 12b & d) with anomalies greater than 10 m s⁻¹ ahead of the disturbance. The Sahel/tropical Africa dryline boundary is located around 19°N, well north to directly influence conditions over the maximum site. Over time, precipitable water increases in the site region as there is a build-up of low-level moisture wrapping around the approaching disturbance.

CASE10 (Fig. 12e) is associated with two mid-level disturbances near southwestern Mali. The first is centered at 4°W and 11°N. It lies in the southern African wave storm track, with cyclonic flow that enhances the atmospheric moisture transport over southern and western Burkina Faso. The second disturbance is stronger and located west of the first disturbance at 6°W and 20°N in the northern African wave storm track. Cyclonic flow associated with the lead disturbance promotes increased equatorward flow of dry western Sahel air ahead of the trailing disturbance, shifting the dryline frontal boundary southward closer to 17°N, while enhancing the vertical zonal wind shear westward to the coast by up to 10 m s⁻¹ (Fig. 12f). Combined, these two disturbances enhance the low to mid-level convergence over southwestern Mali.

Figure 13 shows Hovmöller plots of the 700 hPa relative vorticity and precipitable water anomalies for CASE02 (Figs. 13a & b), CASE07 (Figs. 13c & d), and CASE10 (Figs. 13e & f). CASE02 (Fig. 13a) is associated with a disturbance that slows over western West Africa, followed by a stronger disturbance propagating at 9 m s⁻¹ a couple of days later. The anticyclonic flow is relatively dry (Fig. 13b) until the second system approaches and wrap around moisture builds over the region. CASE07 (Fig. 13c) is associated with a fairly strong disturbance propagating westward into an anomalously dry environment (Fig. 13d). CASE10 (Fig. 13e) is associated with a weak disturbance that originates on 17 July 2004 around 15°E, and propagates at 9.8 m s⁻¹. Around the time of maximum rainfall intensity, the propagation speed slows to 3.7 m s⁻¹. This slowdown occurs when the system encounters drier (Fig. 13f) anticyclonic flow over far western West Africa. It is not until the stronger, second disturbance reaches the area that the storm sheds the West African coast into the eastern North Atlantic.

These cases indicate the importance of the interaction of anticyclonic ridging along the West African Coast with an approaching disturbance from the east to help build-up the atmospheric moisture over the maximum site location. Persistent coastal anticyclonic ridging can also help slow down the propagating disturbances as they move west of 7°W, as was the case for CASE02 (Fig. 13a) and CASE10 (Fig. 13e). Finally, this scenario is found equally likely to be associated with short duration/ high peak intensity (CASE10) and long duration/weaker peak intensity (CASE02) events.

4.3.3 Interaction of the storm in the wake of a region of anticyclonic flow and the Sahel/tropical Africa dryline boundary

Fig. 14 shows ERA5 700 hPa geopotential height, wind, precipitable water, and vertical wind shear anomalies for select times of the CASE04 (Fig. 14a & b), CASE05 (Fig. 14c & d), CASE08 (Fig. 14e & f), and CASE09 (Fig. 14g & h) events. CASE04 and CASE08 are short duration/ high peak intensity events, while CASE09 is a long duration/ weaker peak intensity event, and CASE05 is neither.

CASE04 (Fig. 14a) occurs over north-central Nigeria with a disturbance to the east near 15°N and 20°E. The environment is anomalously wet in the vicinity and upstream of the disturbance, with

precipitable water anomalies 5 – 10 mm greater than normal. Vertical wind shear (Fig. 14b) is only modestly stronger, generally less than 3 m s⁻¹, and confined to a narrow region along the Niger/Nigeria border. Unlike prior scenarios, the Sahel/tropical Africa dryline boundary is now in close proximity to the maximum site and is more directly influential. Mid-level flow is anticyclonic over Niger and relatively drier Sahelian air extends equatorward into southern Niger north of the dryline, setting up a scenario with enhanced low-level convergence south of the dryline frontal boundary over northern Nigeria. The importance of the dryline for the development of convection in this region is consistent with results from other studies (Vizy and Cook 2018, 2019a).

CASE05 (Fig. 14c) is associated with a strong disturbance moving westward along the southern AEW storm track. Ahead of this disturbance, the environment is much drier than normal due in part to anticyclonic ridging along the West African Coast, as well as the southward entrainment of dry Saharan air by the northerly low- to mid-level flow ahead of the disturbance, the latter of which is associated with the southward shift of the dryline boundary closer to the maximum site. Vertical wind shear (Fig. 14d) is 9 - 15 m s⁻¹ stronger over and ahead of the maximum site location.

CASE08 (Fig. 14e) also occurs over north-central Nigeria, and is associated with an approaching disturbance from the east that is not particularly strong. The environment is anomalously wet by 5-10 mm in the vicinity and upstream, while the vertical wind shear (Fig. 14f) is only modestly stronger along the Niger/Nigeria border. The dryline boundary is within 1° of latitude of the maximum site.

CASE09 (Fig. 14g) is similar to CASE05, as it is associated with a westward moving disturbance with anomalous northwesterly flow ahead of the disturbance that entrains drier air southward in close proximity to the maximum site. Vertical wind shear (Fig. 14h) is anomalously stronger ahead of the disturbance by $6 - 15 \text{ m s}^{-1}$.

Fig. 15 shows hovmöller plots of the 700 hPa relative vorticity and precipitable water anomalies averaged between 10°N - 15°N for the cases. CASE04 (Fig. 15a) is associated with two disturbances, with the first one propagating faster than the second one. The maximum rainfall site occurs west of the second disturbance when the anticyclonic flow is transitioning to cyclonic flow and the atmospheric moisture

content begins to increase (Fig. 15b). CASE05 (Fig. 15c) is associated with a fairly strong disturbance propagating westward at 8.3 m s⁻¹ into an anomalously dry environment, with strong anticyclonic flow and drier atmospheric conditions (Fig. 15d) preceding it. CASE08 (Fig. 15e) is associated with a disturbance propagating at 7.1 m s⁻¹. While the peak rainfall intensity occurs when the circulation is only starting to become cyclonic, the environment is relatively moist even when the flow is slightly anticyclonic between 18 – 21 July 2001 (Fig. 15f). The CASE09 disturbance (Fig. 15g) is slower moving (6.2 m s⁻¹) and shorter lived compared to the other three events. This disturbance is associated with an anomalous build-up of atmospheric moisture following an anomalously dry period (Fig. 15h), consistent with the other events.

Overall, these extreme events vary from the previous scenario in that the Sahel/tropical Africa dryline is now influential. The dryline enhances the atmospheric environment making it more likely for convection to organize and develop into a MCS in the vicinity of the maximum sites.

5. Summary and Conclusions

Extreme rainfall events associated with organized convective activity over the West African Sahel/Soudan often resulting in flooding and adverse consequences for the population. A better understanding of the types of storms that deliver these high rainfall amounts, including the environmental conditions in which they form, is needed to improve short-term and climate-scale prediction. 100 storms that delivered the highest 24-hour rainfall totals during the 2000-2019 period over the West African Sahel/Soudan (8.05°W – 12.95°E; 12.05°N – 17.95°N) are examined using NASA satellite-derived rainfall estimates of IMERG and the ERA5 atmospheric reanalysis data. The preferred locations for these extreme events are identified, along with the regions in which the disturbances originate. We examine the mechanisms of storm intensification, including the importance of environmental conditions such as moisture preconditioning and vertical wind shear. We focus on heavy rainfall events on sub-diurnal times scales; multiple-day heavy rainfall events are not considered in this study.

5.1 Summary of top 100 analysis

Examination of the distribution curve of the top 100 maximum 24-h rainfall totals in IMERG (Fig. 2a) indicates that the wettest event having a maximum of 291 mm, with totals decreasing exponentially, meaning that a top 100 event is 7.5 times more likely to be less than 200 mm rather than greater than 200 mm. Seasonally, 83 of the top 100 events occur in July and August coinciding with the peak wet season with no top 100 events during November – March (Fig. 2b).

The 100 selected extreme events are unevenly distributed over the West African Sahel. They are infrequent over the northern Sahel and more common south of 14°N over the Soudan (Fig. 1a). Three regions where events cluster are identified, and each is tied to topography. They are near the Jos Plateau of Nigeria (17 events), the North Mossi Plateau of Burkina Faso (10 events), and the Mandingue Plateau of Mali (24 events). While the elevation changes associated with these features are only around 200 – 400 m, smaller than other orographic features of northern Africa, it is enough and focus the low-level wind convergence and promote some uplift to more consistently result in heavier rainfall events in their proximity.

Most of the MCSs associated with the top 100 events originate between 10°N - 20°N (94 events) with a wide spread in the distance between the genesis and the maximum rainfall location. 25 events form within 100 km of the location of the rainfall maximum, 44 form 100 – 1000 km away, and 31 form more than 1000 km away. In contrast to the location of maximum rainfall, the generation of less than half of the 100 events are associated with elevated terrain (Fig. 1b). The most active storm genesis area extends eastward along the Niger/Nigeria border from 5°E to east of Lake Chad. A variety of factors could explain why genesis is frequent here. For one, the area is a depression that gradually increases in slope westward from Lake Chad that promotes low-level upslope flow that can be important for forming low-level convergence boundaries that support the development and organization of convection. Longitudinally the region lies near 10°E, which is where the influence of low-level summer inflow of moisture from the Gulf of Guinea becomes more influential due to the shape of the continent, so there is a healthy moisture supply here. Latitudinally, the area lies in close proximity of where the AEW southern storm track is typically

positioned meaning there are frequent atmospheric disturbances that traverse the region. The area is also just downstream of Lake Chad, which could also be influential as a moisture source and/or generating low-level convergence boundaries to help important for the development and organization of convection. Future work beyond this study is needed to better understand the relative roles of these above-mentioned factors.

Size of the 24-h rainfall totals exceeding 100 mm for most of the top 100 events is localized with areal coverage around 4,000 km² or less (Fig. 3). For the 12 events large in size (> 20,000 km²), half fall in the top 10 in terms of maximum 24-h total rainfall (Table 1), indicating that the top 10 events are more likely to be more impactful in terms of flooding potential at larger spatial scales. This is confirmed by cross-referencing with available FEWSNET reports, CRED EM-DAT disaster reports, OCHA Reliefweb, DREF bulletin reports, and any available extreme rainfall studies, as 9 of the top 10 events are associated with impactful flooding events (Table 2).

Composites formed from the top 100 events are used to better understand the atmospheric environmental conditions associated with these extreme cases. They are associated with a significant and widespread increase in precipitable water over the entire Sahel prior to the event (Fig. 4b). There is no evidence of a consistent or large change in the 600– 925 hPa vertical wind shear (Fig. 4d) in association with this region's extreme rainfall events. This is consistent with Olaniyan et al. (2021), who also finds that vertical wind shear has a much weaker impact on higher precipitation totals than moisture availability for extreme rainfall events over Nigeria. In contrast, Taylor et al. (2017) and Klein et al. (2021) find that stronger wind shear is associated with more intense MCSs over West Africa. However, this difference can be understood when considering the methodology differences between the studies. In our study, we use 24-h total accumulated IMERG rainfall estimates to identify the top 100 extreme rainfall events selected for analysis. However, Taylor et al. (2017) and Klein et al. (2021) use Meteosat satellite cloud top temperature data to quantify the development of the MCSs, as cloud-top temperatures are commonly used to estimate updraft velocities/convective intensity of the systems (Cecil et al. 2005; Zipser et al. 2006). While this method identifies extreme weather systems with strong convective updrafts that extend to high altitudes, it does not necessarily translate into extreme rainfall rates at the surface, as the heaviest rainfall

events are mostly found to be associated with less intense convection as excess low-level moisture leads to a higher efficiency in the growth of precipitation-sized hydrometeors (Hamada et al. 2015).

5.2 Summary of top 10 analysis

- The top 10 events are individually examined to evaluate storm development for the most extreme events. Analysis indicates that these events are found to be associated with one of the following three atmospheric conditions:
- #1: Moisture preconditioning of the atmosphere: (CASE01, CASE03, CASE06): For CASE03 the enhanced moisture is associated with the passage of a preceding disturbance a day earlier that increases the atmospheric moisture west of 8°E starting on 24 August 2007 (Fig. 11d). For CASE01 (Fig. 11b) and CASE06 (Fig. 11f) conditions are anomalously wet across the entire Sahel/Soudan for the entire 10-day analysis window. For these two cases the MJO may be influential. Inspection of the Daily Multivariate MJO Index provided by the Australian Government Bureau of Meteorology (Australian Bureau of Meteorology 2021) indicates that these two events are associated with a relatively strong MJO wet phase over tropical northern Africa. Past studies have indicated that boreal summer convective activity over West Africa and the Sahel increases during these phases as the associated circulation patterns enhance moisture loading over the West Africa Sahel and destabilize the environment (Matthews 2004; Janicot et al. 2009; Alaka Jr and Maloney 2012, 2014; Schlueter et al. 2019a,b).
- #2: Interaction of the storm in the wake of a region of anticyclonic flow (CASE02, CASE07, CASE10): A westward moving disturbance draws moisture into the system from the south and west even as the system moves into an anomalously dry large-scale environment dominated by anticyclonic flow. In two cases (CASE02 and CASE10; Figs. 13a and 13e), the systems slow as they approach anticyclonic ridging along the coast. This slow-down is consistent with a deceleration and/or temporary stalling of the wave disturbances observed over West Africa (Cornforth et al. 2017; Engel et al. 2017). The relatively close proximity of the coast also could be a factor (Reed et al. 1977; Thorncroft and

Hodges 2001; Berry and Thorncroft 2005; Berry et al. 2007; Hamilton et al. 2017). Here, coastal ridging remains persistent and slow to break down (Figs. 13a and 13e) contributing to the deceleration of the disturbance as it approaches from the east. More work is needed to better understand the extent to which ridging varies and how this impacts the propagation of approaching disturbance.

#3: Interaction of the storm in the wake of a region of anticyclonic flow and the Sahel/tropical Africa dryline boundary (CASE04, CASE05, CASE08, CASE09): This scenario is a variant of pattern #2 that involves interactions with the dryline. Approaching disturbances draw tropical moisture northward into a developing system, while anticyclonic northerly/northwesterly flow ahead of the system displaces the Sahel/tropical Africa dryline boundary equatorward and enhances the southward infiltration of drier Sahelian air into the region. This circulation pattern results in an area of enhanced low-level convergence and an unstable environment ahead of the approaching disturbance in the area where the heavy rainfall is observed to occur. Past studies (Vizy and Cook 2018, 2019a) have shown that the Sahel/tropical Africa dryline can be a key environmental factor for the development of strong convection over the Sahel.

5.3 Conclusions

This study identifies anomalously high atmospheric moisture content as an important environmental condition for the development of extreme rainfall events over the West African Sahel and Soudan. Unlike some previous studies we do not find that large-scale vertical wind shear, for example, in association with the African easterly jet, plays an essential role. Of the top 100 events analyzed, only a little over half form in an anomalously strong vertical wind shear environment. While 8 of the top 10 events are associated with anomalously high vertical wind shear, the shear is localized and cause-and-effect is not discernible (Figs. 10, 12, and 14). A composite of the top 100 24-hr rain-producing events population does not show an association with vertical shear prior to the event (Fig. 4), so vertical wind shear is not a good predictor of an extreme rainfall event over the West African Sahel.

On climate change (decadal) time scales, these results suggest that increases in atmospheric moisture associated with surface warming, e.g., through the Clausius-Clapeyron relation, provide a mechanism for storm intensification. The large-scale vertical shear environment over the Sahel is observed to be changing - the mid-tropospheric African easterly jet is intensifying as large-scale meridional temperature gradients increase in association with amplified warming over the Sahara (Cook and Vizy 2015; Vizy and Cook 2017). The current results indicate that this intensification in the jet will not serve as a mechanism for storm intensification. However, additional research is needed to confirm this result and understand how localized shear impacts storm development.

Acknowledgements: This work was funded by NSF Award #1929074. The authors acknowledge the Texas Advanced Computing Center (TACC) at The University of Texas at Austin for providing HPC and database resources that have contributed these research results URL: http://www.tacc.utexas.edu. The Grid Analysis and Display System software (GrADS) developed at COLA/IGES was used for generating the figures.

735 References 736 Adeoye NO, Ayanlade A, Babatimehin O (2009) Climate change and menace floods in Nigerian cities: Socio-economic implications. Adv in Nat Appl Sci 3: 369-377. 737 Alaka Jr GJ, Maloney ED (2012) The influence of the MJO on upstream precursors to African easterly 738 739 waves. J Clim 25: 3219 – 3236. https://doi.org/10.1175/JCLI-D-11-00232.1 Alaka Jr GJ, Maloney ED (2014) The intraseasonal variability of African easterly wave energetics. J Clim 740 741 27: 6559 – 6580. https://doi.org/10.1175/JCLI-D-14-00146.1 American Meteorological Society (2021) Intertropical front. Glossary Meteorology. 742 https://glossary.ametsoc.org/wiki/Intertropical front 743 Anash SO, Ahiatahu MA, Yorke CK, Out-Larbi F, Yahaya B, Lamptey PNL, Tanu M (2020) 744 Meteorological analysis of floods in Ghana. Advances in Meteorol 4230627: 1 - 14. 745 https://doi.org/10.1155/2020/4230627 746 747 Australian Bureau of Meteorology (2021)Madden-Julian Oscillation. http://www.bom.gov.au/climate/mjo/. Accessed 25 Feb 2021. 748 Barnes GM, Sieckman K (1984) The environment of fast- and slow-moving tropical mesoscale convective 749 750 1782–1794. https://doi.org/10.1175/1520cloud lines. Mon Wea Rev 112: 751 0493(1984)112,1782:TEOFAS.2.0.CO;2 752 Berry G, Thorncroft C (2005) Case study of an intense African easterly wave. Mon Wea Rev 133: 752-766. 753 https://doi.org/10.1175/MWR2884.1 Berry G, Thorncroft C, Hewson T (2007) African easterly waves during 2004 – Analysis using objective 754 techniques. Mon Wea Rev 135: 1251-1267. https://doi.org/10.1175/MWR3343.1 755 Burpee RW (1972) The origin and structure of easterly waves in the lower troposphere of North Africa. J 756 Atmos Sci 29: 77-90. https://doi.org/10.1175/1520-0469(1972)029<0077:TOASOE>2.0.CO;2 757 758 Carlson TN (1969a) Synoptic histories of three African disturbances that developed into Atlantic 759 hurricanes. Mon Wea Rev 97: 256-276. https://doi.org/10.1175/1520-0493(1969)097,0256:SHOTAD.2.3.CO;2 760

761	Carlson TN (196	9b) Some rer	narks on Afr	rican disturb	pances and their pr	ogress over the t	ropical Atlantic.
762	Mon	Wea	Rev	97:	716–726.	https://doi.org	g/10.1175/1520-
763	0493(196	59)097<0716	SROADA>2	2.3.CO;2			
764	Carlson TN, Ber	njamin SG,	Forbes GS	(1983) Ele	vated mixed laye	rs in the regions	al severe storm
765	environm	nent: concep	tual model	and case	studies. Mon	Weather Rev	111:1453–1473.
766	https://do	oi.org/10.1175	5/1520-0493	(1983)111<	1453:EMLITR>2.	0.CO;2	
767	Cecil DJ, Goodm	an SJ, Bocci	ppio DJ, Zip	ser EJ, Nes	oitt SW (2005) Th	ree years of TRM	IM precipitation
768	features.	Part I: Rada	r, radiometr	ric, and light	ning characteristic	es. Mon Wea Rev	v 133: 543–566.
769	https://do	oi.org/10.1175	5/MWR-287	<u>6.1</u> .			
770	Cook KH (1997)	Large-scale	atmospheric	dynamics a	nd Sahelian precip	itation. J Climate	: 10: 1137-1152.
771	https://do	oi.org/10.1175	5/1520-0442	(1997)010<	1137:LSADAS>2.	<u>.0.CO;2</u>	
772	Cook KH (2015)	Role of inter	tial instabili	ty in the We	est African monsoo	on jump. J Geoph	ys Res – Atmos
773	120: 308:	5-3102. <u>https</u>	s://doi.org/10	0.1002/2014	JD022579		
774	Cook KH, Vizy I	EK (2015) De	etection and	analysis of	an amplified warn	ning of the Sahara	a Desert. J Clim
775	28: 6560-	-6580. <u>https:/</u>	/doi.org/10.1	<u> 175/JCLI-I</u>	D-14-00230.1		
776	Copernicus Clim	ate Change	Service (C3	3S) (2020)	ERA5: Fifth gene	eration of ECMV	VF atmospheric
777	reanalyse	es of the glob	al climate. (Copernicus (Climate change Se	rvice Climate Da	ata Store (CDS),
778	Accessed	1 June 2020	. https://cds.	climate.cop	ernicus.edu/cdsapp	#!/home	
779	Cornforth RJ, Mu	ımba Z, Park	er DJ, et al ((2017) Syno	ptic systems. Mete	orology of Tropic	cal West Africa:
780	The Fore	ecasters' Har	dbook, D.	J. Parker aı	nd M. Diop-Kane	, Eds., Wiley-Bla	ackwell, 40–89,
781	https://do	oi.org/10.1002	2/978111839	91297.ch2			
782	Danso DK, Anqu	etin S, Diedl	niou A, Lava	ysse C, Koł	oea A, Touré NE (2019) Spatio-tem	poral variability
783	of cloud	cover types in	West Africa	a with satelli	te-based and reana	ılysis data. QJR	oy Meteorol Soc
784	145: 371:	5-3731. <u>https</u>	://doi.org/10	.1002/qj.36	<u>51</u>		
785	Desbois M., Kayi	iranga T, Gna	amien B, Gu	essous S, Pi	con L (1988) Cha	racterization of so	ome elements of
786	the Sahe	lian climate	and their in	terannual v	ariations for July	1983, 1984, and	1985 from the

787	analysis of Meteosat ISCCP data. J Clim 9: 867–904. https://doi.org/10.1175/1520-
788	<u>0442(1988)001<0867:COSEOT>2.0.CO;2</u>
789	Dezfuli AK, Ichoku CM, Huffman GJ, Mohr KI, et al (2017) Validation of IMERG precipitation in Africa.
790	J Hydrometeorol 18: 2817 – 2825. https://doi.org/10.1175/JHM-D-17-0139.1
791	Di-Baldassarre G, Montanari A, Lins H, Koutsoyiannis D, Brandimarte L, Blöschl G (2010) Flood fatalities
792	in Africa: From diagnosis to mitigation. Geophys Res Lett 37: 1 - 5.
793	https://doi.org/10.1029/2010GL045467
794	Diehiou A, Janicot S, Viltard A, de Felice P, Laurent H (1999) Easterly wave regimes and associated
795	convection over West Africa and tropical Atlantic: Results from the NCEP/NCAR and ECMWF
796	reanalyses. Clim Dyn 15: 795-822. https://doi.org/10.1007/s003820050316
797	Dione C, Lothon M, Badiane D, Campistron B, Couvreux F, Guichard F, Salle S (2014) Phenomenology
798	of Sahelian convection observed in Niamey during the early monsoon. Q J R Meteorol Soc
799	140:500–516. https://doi.org/10.1002/qj.2149
800	Doswell CA III, Brooks HE, Maddox RA (1996) Flash flood forecasting: An ingredients-based
801	methodology. Wea Forecasting 11: 560-581. https://doi.org/10.1175/1520-
802	<u>0434(1996)011<0560:FFFAIB>2.0.CO;2</u>
803	Douglas I, Alam K, Maghenda M, McDonnell Y, McLean L, Campbell J (2008) Unjust waters: Climate
804	change, flooding and the poor in Africa. Environ Urban 20: 187-205.
805	https://doi.org/10.1177/0956247808089156
806	Duvel J-P (1989) Convection over tropical Africa and the Atlantic Ocean during northern summer. Part I:
807	Interannual and diurnal variations. Mon Wea Rev 117: 2782–2799. https://doi.org/10.1175/1520-
808	<u>0493(1989)117<2782:COTAAT>2.0.CO;2</u>
809	Eldridge RH (1957) A synoptic study of West African disturbance lines. Q J Roy Meteorol Soc 83: 303 –
810	314. <u>https://doi.org/10.1002/qj.49708335704</u>
811	EM-DAT (2020) EM-DAT: The OFDA/CRED International Disaster Database, https://www.emdat.be/ ,

813	Engel T, Fink AH, Knippertz P, Pante G (2017) Extreme precipitation in the West African cities of Dakar
814	and Ouagadougou: Atmospheric dynamics and implications for flood risk assessments. J
815	Hydrometeorol 18: 2937-2957. https://doi.org/10.1175/JHM-D-16-0218.1
816	FEWS NET (2020) The Famine Early Warning System Network, USAID, https://fews.net/ , accessed 15
817	May 2020.
818	Fink AH, Reiner A (2003) Spatiotemporal variability of the relation between African easterly waves and
819	West African squall lines in 1998 and 1999. J Geophys Res 108: 4332.
820	https://doi.org/10.1029/2002JD002816
821	Fink AH, Vincent DG, Ermert V (2006) Rainfall types in the West African Sudanian zone during the
822	summer monsoon 2002. Mon Weather Rev 134:2143–2164.
823	https://doi.org/10.1175/MWR3182.1Fitzpatrick RGJ., Parker DJ, Marsham JH, Rowell DP,
824	Guichard FM, Taylor CM, Cook KH, Vizy EK, Jackson LS, Finney D, Crook J, Stratton R, and
825	Tucker S (2020) What drives the intensification of mesoscale convective systems over the West
826	African Sahel under climate change? J Climate 33: 3151-3172. https://doi.org/10.1175/JCLI-D-
827	<u>19-0380.1</u>
828	Galvin JFP (2010) Two easterly waves in West Africa in summer of 2009. Weather 65: 219-227.
829	https://doi.org/10.1002/wea.605
830	Gaona MFR, Overeem A, Leijnse H, Uijlenhoet R (2016) First-year evaluation of GPM rainfall over The
831	Netherlands: IMERG day 1 final run (V03D). J Hydrometeor 17: 2799–2814.
832	https://doi.org/10.1175/JHM-D-16-0087.1
833	Giorgi F, Im E-S, Coppola E, Diffenbaugh NS, Gao XJ, Mariotti L, Shi Y (2011) Higher hydroclimatic
834	intensity with global warming. J Clim 24: 5309-5324. https://doi.org/10.1175/2011JCLI3979.1
835	Hagos S, Zhang C Diabatic heating, divergent circulation and moisture transport in the African monsoon
836	system. Quart J Roy Meteorol Soc 136: 411-425. https://doi.org/10.1002/qj.538
837	Hamada A, Takayabu YN, Liu C, Zipser EJ (2015) Weak linkage between the heaviest rainfall and tallest
838	storms. Nat. Commun. 6: 6213. https://doi.org/10.1038/NCOMMS7213.

839 840	
841	Hamilton HL, Young GS, Evans JL, Fuentes JD, Núñez Ocasio KM (2017) The relationship between the
842	Guinea Highlands and the West African offshore rainfall maximum. Geophys Res Lett 44: 1158-
843	1166. https://doi.org/10.1002/2016GL071170
844	Hamilton RA, Archbold (1945) Meteorology of Nigeria and adjacent territory. Quart J Roy Meteorol Soc
845	71: 231-264. https://doi.org/10.1002/qj.49707130905
846	Han F, Cook KH, Vizy EK (2019) Changes in intense rainfall events and drought across Africa in the 21st
847	century. Clim Dyn 53: 2757-2777. https://doi.org/10.1007/s00382-019-04653-z
848	Hastenrath S, Lamb P (1977) Some aspects of circulation and climate over the eastern equatorial Atlantic.
849	Mon Wea Rev 105: 1019-1023. https://doi.org/10.1175/1520-1019
850	<u>0493(1977)105<1019:SAOCAC>2.0.CO;2</u>
851	Hodges KI, Thorncroft CD (1997) Distribution and statistics of African mesoscale convective weather
852	systems based on ISCCP METEOSAT imagery. Mon Wea Rev 125: 2821- 2837.
853	https://doi.org/10.1175/1520-0493(1997)125<2821:DASOAM>2.0.CO;2
854	Hou AY, and et al (2014) The Global Precipitation Measurement mission. Bull Amer Meteor Soc 95: 701–
855	722. https://doi.org/10.1175/BAMS-D-13-00164.1 .
856	Hsieh J-S., Cook KH (2005) Generation of African easterly wave disturbances: Relationship to the African
857	easterly jet. Mon Wea Rev 133: 1311-1327. https://doi.org/10.1175/MWR2916.1
858	Hsieh J-S., Cook KH (2008) On the instability of the African easterly jet and the generation of African
859	waves: Reversals of the potential vorticity gradient. J Atmos Sci 65: 2130-2151.
860	https://doi.org/10.1175/2007JAS2552.1
861	Huffman GJ, Bolvin DT, Braithwaite D, Hsu K, Joyce R, Kidd C, Nelkin EJ, Sorooshian S, Tran J, Xie P
862	(2020) NASA Global Precipitation Measurement (GPM) Integrated Multi-satellitE Retrievals for
863	GPM (IMERG). Algorithm Theoretical Basis Doc., version 6.3, 30 pp.,
864	https://gpm.nasa.gov/sites/default/files/2020-05/IMERG ATBD V06.3.pdf

865	Janicot S, Mounier F, Hall NMJ, Leroux S, Sultan B, Kiladis GN (2009) The West African Monsoon			
866	dynamics. Part IV: Analysis of the 25-90 day variability of convection and the role of the Indian			
867	Monsoon. J Clim 22: 1541-1565.			
868	Janicot S, and Coauthors, 2011: Intraseasonal variability of the West African monsoon. Atmos Sci Lett 12:			
869	58–66. <u>https://doi.org/10.1002/asl.280</u>			
870	Kendon EJ, Stratton RA, Tucker S, Marsham JH, Berthou S, Rowell DP, Senior CA (2019) Enhanced future			
871	changes in wet and dry extremes over Africa and convection-permitting scale. Nat Commun 10:			
872	1794. https://doi.org/10.1038/s41467-019-09776-9			
873	Kidd C, Levizzani V (2011) Status of satellite precipitation retrievals. Hydrol Earth Syst Sci 15: 1109-			
874	1116. https://doi.org/10.5194/hess-15-1109-2011			
875	Klein C, Nkrumah F, Taylor CM, Adefisan EA (2021) Seasonality and trends of drivers of mesoscale			
876	convective systems in southern West Africa. J Climate 34: 71 – 87. https://doi.org/10.1175/JCLI-			
877	<u>D-20-0194.1</u>			
878	Knippertz P, Martin JE (2005) Tropical plumes and extreme precipitation in subtropical and tropical West			
879	Africa. Q J R Meteorol Soc 131: 2337-2365. https://doi.org/10.1256/qj.04.148			
880	Kundzewicz ZW, Kanae S, Seneviratne SI, Handmer J, et al (2014) Flood risk and climate change: Global			
881	and regional perspectives. Hydrological Sciences Journal 59: 1 - 28.			
882	https://doi.org/10.1080/02626667.2013.857411			
883	Laing AG, Fritsch JM (1993) Mesoscale convective complexes in Africa. Mon Wea Rev 121: 2254–2263.			
884	https://doi.org/10.1175/1520-0493(1993)121<2254:MCCIA>2.0.CO;2			
885	Laing AG, Fritsch JM, Negri AJ (1999) Contribution of mesoscale convective complexes to rainfall in			
886	Sahelian Africa: Estimates from geostationary infrared and passive microwave data. J Appl			
887	Meteorol 38: 957 – 964. <a href="https://doi.org/10.1175/1520-0450(1999)038<0957:COMCCT>2.0.CO;2">https://doi.org/10.1175/1520-0450(1999)038<0957:COMCCT>2.0.CO;2			
888	Laing AG, Carbone R, Levizzani V, Tuttle J (2008) The propagation and diurnal cycles of deep convection			
889	in northern tropical Africa. Quart J Roy Meteorol Soc 134: 93–109. https://doi.org/10.1002/qj.194			

890	Laurent H, D'Amato N, Lebel T (1998) How important is the contribution of the mesoscale convective
891	complexes to the Sahelian rainfall? Phys Chem Earth 23: 629 – 633. https://doi.org/10.1016/S0079-
892	<u>1946(98)00099-8</u>
893	Lélé MI, Lamb PJ (2010) Variability of the Intertropical front (ITF) and rainfall over the West African
894	Sudan-Sahel zone. J Climate 23:3984-4004. https://doi.org/10.1175/2010JCLI3277.1
895	Leroux S, Hall NMJ (2009) On the relationship between African easterly waves and the African easterly
896	jet. J Atmos Sci 66: 2303–2316. https://doi.org/10.1175/2009JAS2988.1
897	Li F, Chavas DR, Reed KA, Dawson II DT (2020) Climatology of severe local storm environments and
898	synoptic-scale features over North America in ERA5 reanalysis and CAM6 simulation. J Climate,
899	https://doi.org/10.1175/JCLI-D-19-0986.1
900	Li Z, Tang G, Hong Z, Chen M, Gao S, Kirstetter P, Gourley JJ, Wen Y, Yami T, Nabih S, Hong Y (2021)
901	Two-decades of GPM IMERG early and final run products intercomparison: Similarity and
902	difference in climatology, rates, and extremes. J Hydrology 594: 125975.
903	https://doi.org/10.1016/j.jhydrol.2021.125975
904	Liu, W, Cook KH, Vizy EK (2019) The role of mesoscale convective systems in the diurnal cycle of rainfall
905	and its seasonality over sub-Saharan Northern Africa. Clim Dyn 52: 729-745.
906	https://doi.org/10.1007/s00382-018-4162-y
907	Mahmoud MT, Al-Zahrani MA, Sharif HO (2018) Assessment of global precipitation measurement satellite
908	products over Saudi Arabia. J Hydrology 559: 1 – 12. https://doi.org/10.1016/j.jhydrol.2018.02.015
909	Magami IM, Yahaya S, Mohammed K (2014) Causes and consequences of flooding in Nigeria: A review.
910	Biological and Environmental Sci J for the Tropics 11: 154-162.
911	Maranan M, Fink AH, Knippertz P, Amekudzi LK, Atiah WA, Stengel M (2020) A process-based
912	validation of GPM IMERG and its sources using a mesoscale rain gauge network in the West
913	African forest zone. J Hydrometeorol 21: 729-749. https://doi.org/10.1175/JHM-D-19-0257.1
914	Marsham JH, Dixon N, Garcia-Carreras L, Lister G, Parker DJ, Knippertz P, Birch C (2013) The role of
915	moist convection in the West African monsoon system—insights from continental-scale

916	convection-permitting simulations. Geophys Res Lett 40: 1843–1849.
917	https://doi.org/10.1002/grl.50347
918	Mathon V, Laurent H, Lebel T (2002) Mesoscale convective system rainfall in the Sahel. J Appl Meteorol
919	41: 1081–1092. https://doi.org/10.1175/1520-0450(2002)041<1081:MCSRIT>2.0.CO;2
920	Matthews AJ (2004) Intraseasonal variability over tropical Africa during northern summer. J Climate 17:
921	2427-2440. https://doi.org/10.1175/1520-0442(2004)017<2427:IVOTAD>2.0.CO;2
922	Mekonnen A, Thorncroft CD, Aiyyer A (2006) Analysis of convection and its association with African
923	easterly waves. J Climate 19: 5405–5421. https://doi.org/10.1175/JCLI3920.1
924	Mohr KI (2004) Interannual, monthly, and regional variability in the wet season diurnal cycle of
925	precipitation in sub-Saharan Africa. J Climate 17: 2441-2453. https://doi.org/10.1175/1520-
926	<u>0442(2004)017<2441:IMARVI>2.0.CO;2</u>
927	Mohr KI, Thorncroft CD (2006) Intense convective systems in West Africa and their relationship to the
928	African easterly jet. Q J Roy Meteorol Soc 132: 163–176. https://doi.org/10.1256/qj.05.55
929	Nair S, Srinivasan G, Nemani R (2009) Evaluation of multi-satellite TRMM derived rainfall estimates over
930	a western state of India. J Meteor Soc Japan 87: 927–939. https://doi.org/10.2151/JMSJ.87.927
931	Nicholson SE, et al (2003) Validation of TRMM and other rainfall estimates with a high-density gauge
932	dataset for West Africa. Part II: Validation of TRMM rainfall products. J Appl Meteor 42: 1355-
933	1368. https://doi.org/10.1175/1520-0450(2003)042,1355:VOTAOR.2.0.CO;2
934	Olaniyan OA, Ajayi VO, Lawal KA, Akeh UP (2021) Impact of Moisture Flux and Vertical Wind
935	Shear on Forecasting Extreme Rainfall Events in Nigeria. In: Leal Filho W., Oguge N., Ayal
936	D., Adeleke L., da Silva I. (eds) African Handbook of Climate Change Adaptation. Springer,
937	Cham. https://doi.org/10.1007/978-3-030-42091-8_98-1
938	Omranian E, Sharif HO (2018) Evaluation of the global precipitation measurement (GPM) satellite rainfall
939	products over the lower Colorado River basin, Texas. J Am Water Resour Assoc 54: 882-898.
940	https://doi.org/10.1111/1752-1688.12610

941	Panthou G, Vischel T, Lebel T (2014) Short Communication: Recent trends in the regime of extreme rainfall
942	in the Central Sahel. Int J Climatol 34: 3998-4006. https://doi.org/10.1002/joc.3984
943	Parker DJ, Burton RR, Diongue-Niang A, Ellis RJ, Felton M, Taylor CM, Thorncroft CD, Bessemoulin P,
944	Tompkins AM (2005) The diurnal cycle of the West African monsoon circulation. Quart J Roy
945	Meteorol Soc 131: 2839–2860. https://doi.org/10.1256/qj.04.52
946	Peters M. Tetzlaff G (1988) The structure of West African squall lines and their environmental moisture
947	budget. Meteorol Atmos Phys 39: 74 – 84. https://doi.org/doi:10.1007/BF01041933
948	Pfeifroth U, Mueller R, Ahrens B (2013) Evaluation of satellite-based and reanalysis precipitation data in
949	the tropical Pacific. J Appl Meteor Climatol 52: 634-644. https://doi.org/10.1175/JAMC-D-12-
950	<u>049.1</u>
951	Pfeifroth U, Trentmann J, Fink AH, Ahrens B (2016) Evaluating satellite-based diurnal cycles of
952	precipitation in the African tropics. J Applied Meteorol Climatol 55: 23-38.
953	https://doi.org/10.1175/JAMC-D-15-0065.1
954	Provod M, Marsham JH, Parker DJ, Birch CE (2016) A characterization of cold pools in the West African
955	Sahel. Mon Weather Rev 144: 1924–1934. https://doi.org/10.1175/MWR-D-15-0023.1
956	Rajagopal M, Zipser E, Huffman G, Russell J, Tan J (2021) Comparison of IMERG version 06 precipitation
957	at and between passive microwave overpasses in the tropics. J Hydrometeorol 22: 2117-2130.
958	https://doi.org/10.1175/JHM-D-20-0226.1
959	Redelsperger JL, Lafore JP (1988) A three-dimensional simulation of a tropical squall-line: convective
960	organization and thermodynamic vertical transport. J Atmos Sci 45:1334-1356.
961	https://doi.org/10.1175/1520-0469(1988)045<1334:ATDSOA>2.0.CO;2
962	Reed RJ, Norquist DC, Recker EE (1977) The structure and properties of African wave disturbances as
963	observed during Phase III of GATE. Mon Wea Rev 105: 317-333. https://doi.org/10.1175/1520-
964	<u>0493(1977)105<0317:TSAPOA>2.0.CO;2</u>
965	Roca R, Chambon P, Jobard I, Kirstetter P-E, Gosset M, Bergès JC (2010) Comparing satellite and surface
966	rainfall products over West Africa at meteorologically relevant scales during the AMMA campaign

967	using error estimates. J Appl Meteor Climatol 49: 715-731.
968	https://doi.org/10.1175/2009JAMC2318.1
969	Rotunno R, Klemp JB, Weisman ML (1988) A theory for strong, long-lived squall lines. J Atmos Sci
970	45:463-485. https://doi.org/10.1175/1520-0469(1988)045<0463:ATFSLL>2.0.CO;2
971	Rowell DP, Milford JR (1993) On the generation of African squall lines. J Clim 6: 1181-1193.
972	https://doi.org/10.1175/1520-0442(1993)006<1181:OTGOAS>2.0.CO;2
973	Samimi C, Fink AH, Paeth H (2012) The 2007 flood in the Sahel: Causes, characteristics and its
974	presentation in the media and FEWS NET. Nat Hazards Earth Syst Sci 12: 313-325.
975	https://doi.org/10.5194/nhess-12-313-2012
976	Schlueter A, Fink AH, Knippertz P, Vogel P (2019a) A systematic comparison of tropical waves over
977	Northern Africa. Part I: Influence on rainfall. J Clim 32: 1501-1523. https://doi.org/10.1175/JCLI-
978	<u>D-18-0173.1</u>
979	Schlueter A, Fink AH, Knippertz P (2019b) A systematic comparison of tropical waves over Northern
980	Africa. Part II: Dynamics and thermodynamics. J Clim 32: 2605-2625.
981	https://doi.org/10.1175/JCLI-D-18-0651.1
982	Tapiador FJ, Navarro A, et al (2020) The contribution of rain gauges in the calibration of IMERG product:
983	Results from the first validation over Spain. J Hydrometeorol 21: 161-182.
984	https://doi.org/10.1175/JHM-D-19-0116.1
985	Tarhule A (2005) Damaging rainfall and flooding: The other Sahel hazards. Climatic Change, 72, 355–377.
986	https://doi.org/10.1007/s10584-005-6792-4
987	Taylor CM (2010) Feedbacks on convection from an African wetland. Geophys Res Lett 37: L05406.
988	https://doi.org/10.1029/2009GL041652
989	Taylor CM, Belušić D, Guichard F, Parker DJ, Vischel T, Brock O, Harris PP, Janicot S, Klien C, Panthou
990	G (2017) Frequency of extreme Sahelian storms tripled since 1982 in satellite observations. Nature
991	544: 475-478, https://doi.org/10.1038/nature22069

992	Taylor CM, Birch CE, Parker DJ, Dixon N, Guichard F, Nikulin G, Lister GMS (2013) Modeling soil
993	moisture-precipitation feedback in the Sahel: Importance of spatial scale versus convective
994	paramterization. Geophys Res Lett 40: 6213-6218. https://doi.org/10.1002/2013GL058511
995	Taylor CM, de Jeu RAM, Guichard F, Harris PP, Dorigo WA (2012) Afternoon rain more likely over drier
996	soils. Nature 489: 423-426. https://doi.org/10.1038/nature11377
997	Taylor CM, Prigent C, Dadson SJ (2018) Mesoscale rainfall patterns observed around wetlands in sub-
998	Saharan African. Q J R Meteorol Soc 144: 2118-2132. https://doi.org/10.1002/qj.3311
999	Tetzlaff G, Peters M (1988) A composite study of early summer squall lines and their environment over
1000	West Africa. Meteorol Atmos Phys 38: 153–163. <u>https://doi.org/10.1007/BF01029779</u>
1001	Thorncroft C, Hodges K (2001) African easterly wave variability and its relationship to Atlantic tropical
1002	cyclone activity. J Climate 14: 1166–1179. https://doi.org/10.1175/1520-
1003	<u>0442(2001)014<1166:AEWVAI>2.0.CO;2</u>
1004	Thorncroft CD, Ngyyen H, Zhang C, Peyrillé P (2011) Annual cycle of the West African monsoon:
1005	Regional circulations and associated water vapour transport. Quart J Roy Meteorol Soc 137: 129-
1006	147. https://doi.org/10.1002/qj.728
1007	Tramblay Y, Villarini G, Zhang W (2020) Observed changes in flood hazard in Africa. Environ Res Lett
1008	15: 1040b5. https://doi.org/10.1088/1748-9326/abb90b
1009	Trier SB, Chen F, Manning KW (2004) A study of convective initiation in a mesoscale model using high-
1010	resolution land surface initial conditions. Mon Wea Rev 132: 2954–2976.
1011	https://doi.org/10.1175/MWR2839.1
1012	Trier SB, Romine GS, Ahuevych DA (2015) Mesoscale thermodynamic influences on convection initiation
1013	near a surface dryline in a convection-permitting ensemble. Mon Wea Rev 143:3726-3753.
1014	https://doi.org/10.1175/MWR-D-15-0133.1
1015	Tschakert P, Sagoe R, Ofori-Darko G, Codjoe SN (2010) Floods in the Sahel: An analysis of anomalies,
1016	memory, and anticipatory learning. Climatic Change 103: 471-502.
1017	https://doi.org/10.1007/s10584-009-9776-y

1018	Vizy EK, Cook KH (2017) Seasonality of the observed amplified Sahara warming frend and implications
1019	for Sahel rainfall. J Clim 30: 3073-3094. https://doi.org/10.1175/JCLI-D-16-0687.1
1020	Vizy EK, Cook KH (2018) Mesoscale convective systems and nocturnal rainfall over the West African
1021	Sahel: Role of the Inter-tropical front. Clim Dyn 50: 587-614. https://doi.org/10.1007/s00382-017-
1022	<u>3628-7</u>
1023	Vizy EK, Cook KH (2019a) Understanding the summertime diurnal cycle of precipitation over sub-Saharan
1024	West Africa: Regions with daytime rainfall peaks in the absence of significant topographic features.
1025	Clim Dyn 52: 2903-2922. https://doi.org/10.1007/s00382-018-4315-z
1026	Vizy EK, Cook KH (2019b) Observed relationship between the Turkana low-level jet and boreal summer
1027	convection. Clim. Dyn 53: 4037 – 4058. https://doi.org/10.1007/s00382-019-04769-2
1028	Vondou DA (2012) Spatio-temporal variability of Western Central African convection from infrared
1029	observations. Atmosphere 3: 377–399. https://doi.org/10.3390/atmos3030377
1030	Wang Z, Zhong R, Lai C, Chen J (2017) Evaluation of the GPM IMERG satellite-based precipitation
1031	products and the hydrological utility. Atmos Res 196: 151-163.
1032	https://doi.org/10.1016/j.atmosres.2017.06.020
1033	Watters D, Battaglia A, Mroz K, Tridon F (2018) Validation of the GPM Version-5 surface rainfall products
1034	over Great Britain and Ireland. J Hydrometeorol 19: 1617-1636. https://doi.org/10.1175/JHM-D-
1035	<u>18-0051.1</u>
1036	Weisman ML, Rotunno R (2004) "A theory for strong long lived squall lines" revisited. J Atmos Sci 61:
1037	361–382. https://doi.org/10.1175/1520-0469(2004)061,0361:ATFSLS.2.0.CO;2
1038	Zahiri E-P, Bamba I, Famien AM, Koffi AK Ochou AD (2016) Mesoscale extreme rainfall events in West
1039	Africa: The cases of Niamey (Niger) and the Upper Ouémé Valley (Benin). Wea and Clim
1040	Extremes 13: 15-34. https://doi.org/10.1016/j.wace.2016.05.001
1041	Zhang G, Cook KH, Vizy EK (2016a) The diurnal cycle of warm season rainfall over West Africa. Part I:
1042	Observational analysis. J Clim 29:8423-8437. https://doi.org/10.1175/JCLI-d-15-0874.1

1043	Zhang G, Cook KH, Vizy EK (2016b) The diurnal cycle of warm season rainfall over West Africa. Part II
1044	Convection-permitting simulations. J Clim 29:8439–8454. https://doi.org/10.1175/JCLI-d-15-
1045	<u>0875.1</u>
1046	Zhao S, Cook KH, Vizy EK (2021) How shrinkage of Lake Chad affects the local climate. Submitted Clim
1047	Dyn.
1048	Zipser EJ (1977) Mesoscale and convective-scale downdrafts as distinct components of squall-line
1049	structure. Mon Wea Rev 105: 1568-1589. https://doi.org/10.1175/1520-0.1568-1589 .
1050	<u>0493(1977)105<1568:MACDAD>2.0.CO;2</u>
1051	Zipser EJ, Cecil DJ, Liu C, Nesbitt SW, Yorty DP (2006) Where are the most intense thunderstorms or
1052	Earth? Bull Amer Meteor Soc 87: 1057–1071. https://doi.org/10.1175/BAMS-87-8-1057.
1053	

Table 1. Listing of the top 100 rainfall events identified for the Sahel analysis region.

CASE		Lon.	Lat.	Total rainfall	Max. Peak Intensity	Duration	Δ Vert. Wind Shear
ID	Date	(°E)	(°N)	(mm)	(mm/h)	(h)	Strength
1	20-21 AUG 2019	9.85	16.15	291.2	77.40	8.0	stronger
2	07-08 AUG 2012	-6.35	12.55	280.8	52.67	19.5	stronger
3	26-27 AUG 2007	-2.25	12.15	262.8	33.82	16.5	weaker
4	06-07 AUG 2001	8.35	12.25	254.3	70.28	10.5	stronger
5	04-05 AUG 2007	-2.55	13.55	242.7	57.99	11.0	stronger
6	23-24 AUG 2019	-6.75	13.65	225.1	30.42	15.5	stronger
7	01-02 SEP 2009	-7.85	13.15	225.0	91.77	12.0	stronger
8	19-20 JUL 2001	9.05	12.45	207.8	80.97	9.5	stronger
9	14-15 JUL 2007	-5.65	13.25	203.1	47.48	15.5	weaker
10	19-20 JUL 2004	-7.75	12.55	197.7	67.61	8.5	stronger
11	03-04 SEP 2010	-7.95	13.65	197.2	57.45	9.5	weaker
12	12-13 AUG 2005	11.35	12.65	192.7	69.01	7.0	weaker
13	28-29 AUG 2007	8.85	15.15	191.0	76.70	7.5	weaker
14	26-27 AUG 2005	-7.25	13.55	188.2	77.43	13.0	stronger
15	22-23 AUG 2006	-4.15	13.45	188.1	55.57	16.5	weaker
16	12-13 JUL 2003	-7.55	13.25	187.9	66.66	6.5	stronger
17	05-06 AUG 2005	11.35	13.65	187.0	60.31	7.5	weaker
18	10-11 AUG 2006	6.25	12.65	185.4	70.99	11.0	stronger
19	14-15 AUG 2008	9.55	12.05	184.9	71.22	8.5	stronger
20	06-07 AUG 2004	-3.15	15.65	182.6	53.88	10.5	stronger
21	03-04 AUG 2006	-0.15	13.75	182.0	68.96	11.0	stronger
22	05-06 OCT 2002	-6.85	13.25	180.4	71.61	13.0	stronger
23	24-25 JUL 2003	-7.95	12.75	178.5	59.38	9.5	weaker
24	08-09 AUG 2001	5.85	16.95	177.2	58.83	4.5	weaker
25	27-28 JUL 2000	8.45	12.85	175.8	51.55	9.0	stronger
26	12-13 AUG 2001	7.65	12.35	173.9	68.26	8.5	stronger
27	20-21 AUG 2013	3.15	13.35	173.6	69.95	9.5	stronger
28	06-07 AUG 2003	-5.15	15.15	172.3	46.79	12.5	stronger
29	13-14 JUL 2006	-7.05	13.15	172.2	39.76	8.5	weaker
30	02-03 AUG 2005	-7.75	12.05	169.8	60.76	7.5	stronger
31	31 AUG - 01 SEP 2009	-1.45	12.65	169.2	59.88	9.5	weaker
32	14-15 AUG 2003	-7.35	12.55	167.8	70.64	12.0	stronger
33	18-19 AUG 2011	-6.55	14.05	167.5	37.13	8.5	weaker
34	07-08 AUG 2004	7.65	12.35	166.8	52.20	10.0	stronger
35	23-24 AUG 2003	-7.55	12.25	165.3	50.86	13.5	stronger
36	05-06 AUG 2019	-7.35	14.25	165.2	51.78	12.0	weaker
37	19-20 OCT 2008	-7.65	12.45	164.7	57.18	7.5	weaker
38	13-14 AUG 2012	9.65	12.05	163.8	59.15	9.5	stronger

39	02-03 AUG 2001	9.95	12.05	163.6	54.51	9.5	stronger
40	19-20 JUL 2000	6.75	12.25	162.9	50.37	11.0	weaker
41	11-12 AUG 2001	9.45	12.15	162.5	50.32	6.5	stronger
42	08-09 JUL 2001	8.45	12.55	162.1	60.75	6.0	weaker
43	19-20 JUL 2010	-7.55	12.95	162.0	40.89	13.5	stronger
44	24-25 AUG 2005	11.65	12.35	162.0	50.20	10.0	stronger
45	18-19 SEP 2010	-8.05	12.85	161.7	55.73	14.0	weaker
46	04-05 AUG 2011	-7.85	14.45	161.5	60.51	8.0	stronger
47	10-11 OCT 2008	-7.85	12.15	161.3	74.00	5.0	weaker
48	31 JUL - 01 AUG 2019	-3.85	12.15	161.0	51.90	11.0	weaker
49	16-17 JUL 2017	6.05	12.05	160.9	52.86	13.5	weaker
50	24-25 AUG 2011	-5.15	12.05	160.1	44.21	12.0	stronger
51	19-20 AUG 2000	7.55	12.45	159.9	49.36	10.0	stronger
52	22-23 AUG 2004	-0.95	12.15	159.5	41.49	10.5	weaker
53	22-23 AUG 2007	7.65	12.75	158.8	48.53	11.5	weaker
54	14-15 AUG 2010	-6.95	13.55	158.6	50.82	9.5	stronger
55	18-19 JUN 2005	8.45	12.15	158.1	43.34	14.0	weaker
56	15-16 AUG 2000	6.45	12.55	157.7	50.60	11.0	stronger
57	07-08 SEP 2008	-5.15	15.25	157.6	42.75	8.5	stronger
58	16-17 SEP 2010	-2.65	12.35	157.3	71.07	9.5	weaker
59	25-26 AUG 2006	-8.05	14.65	157.3	72.45	9.0	weaker
60	20-21 JUL 2004	-7.55	14.15	156.8	59.34	6.5	weaker
61	30-31 JUL 2007	5.55	12.55	156.4	66.85	6.5	weaker
62	17-18 AUG 2001	6.95	12.95	156.3	66.46	11.5	stronger
63	23-24 AUG 2012	-6.75	12.25	155.7	31.69	9.0	stronger
64	18-19 JUL 2008	0.35	12.25	155.4	39.72	17.5	stronger
65	31 JUL-01 AUG 2014	9.95	12.05	155.0	38.99	16.0	stronger
66	23-24 JUL 2000	5.15	12.65	154.8	88.77	4.5	weaker
67	04-05 AUG 2015	-2.25	13.45	154.0	59.58	10.0	weaker
68	02-03 AUG 2003	4.55	12.85	153.6	79.75	8.5	weaker
69	12-13 AUG 2007	3.45	12.05	152.8	69.51	7.0	stronger
70	24-25 AUG 2008	0.95	12.25	152.5	46.06	11.5	weaker
71	26-27 AUG 2004	-4.65	15.05	152.1	58.91	12.0	weaker
72	17-18 AUG 2007	7.15	12.45	151.5	59.53	6.0	weaker
73	25-26 JUL 2003	7.95	12.35	151.5	56.51	7.5	weaker
74	20-21 AUG 2007	-1.55	12.55	151.4	85.78	8.5	stronger
75	27-28 SEP 2006	-1.75	13.25	151.1	67.99	7.0	stronger
76	28-29 JUN 2001	6.35	12.05	151.1	49.33	8.0	weaker
77	17-18 JUL 2003	9.45	12.45	151.1	51.78	10.0	weaker
78	28-29 AUG 2013	2.95	12.15	149.7	59.22	8.0	stronger
79	22-23 AUG 2012	-7.75	12.35	149.1	75.72	7.5	weaker
80	22-23 AUG 2003	6.95	13.35	148.9	71.72	9.0	stronger
81	20-21 AUG 2004	-7.95	14.45	148.6	69.73	8.0	stronger

			St. Dev	28.8	13.5	3.1	_
			Mean	168.4	57.8	9.8	<u>.</u>
100	02-03 JUL 2017	9.85	15.15	138.7	29.23	12.0	stronger
99	28-29 AUG 2011	-7.95	15.65	139.8	65.46	5.5	weaker
98	06-07 JUL 2005	-3.95	15.05	140.5	42.26	9.5	stronger
97	06-07 AUG 2011	-6.55	15.65	141.4	63.31	9.0	stronger
96	23-24 AUG 2011	-7.35	12.85	143.6	61.21	5.0	weaker
95	02-03 JUL 2004	12.55	13.85	144.7	54.87	6.5	weaker
94	05-06 JUL 2001	-7.55	12.95	145.2	46.90	12.5	weaker
93	04-05 JUL 2000	5.45	16.35	145.4	45.79	6.5	weaker
92	08-09 OCT 2008	-7.85	12.95	145.9	76.41	4.5	stronger
91	18-19 SEP 2006	-2.75	15.85	146.0	36.85	10.5	stronger
90	01-02 SEP 2007	5.05	16.25	146.4	64.52	5.0	stronger
89	01-02 AUG 2007	8.25	15.95	146.5	43.98	7.5	weaker
88	06-07 JUN 2005	10.35	13.85	146.5	47.85	10.5	weaker
87	08-09 AUG 2019	-0.55	12.85	146.6	42.99	9.0	stronger
86	31 MAY - 01 JUN 2010	-5.85	12.35	146.8	74.64	9.0	stronger
85	05-06 AUG 2007	-4.45	13.85	147.1	61.39	14.5	stronger
84	08-09 AUG 2016	-1.35	12.75	147.6	34.62	13.5	weaker
83	30 SEP -01 OCT 2003	-7.85	12.35	147.7	71.24	5.5	stronger
82	27-28 JUL 2003	11.65	12.75	148.0	42.85	8.5	weaker

Table 2. Confirmation of high rainfall event impacts from other sources

Event	Date	Source & Relevant Event Information
1	20-21 AUG 2019	FEWSNET – Abundant rains during the weeks have resulted in flooding in
	_, _, _, _,	western Niger and central Mali.
		CRED EM-DAT Disaster # 2019-0394 – 20 Aug – 25 Aug 2019 excessive
		rainfall associated with the same system caused flooding in northern Nigeria
		resulting in 12 deaths and 52,500 people affected
		OCHA Reliefweb – Heavy flooding in during the last weeks of August has
		affected 211,000 people and left 57 dead in central Niger.
2	07-08 AUG 2012	FEWSNET – a northerly position of the intertropical front is associated with
2	07 00 110 0 2012	above average rainfall across Mali and Niger this week.
		OCHA Reliefweb – Heavy August rains responsible for flooding in the southern
		regions of Mali affecting over 9,000 people
3	26-27 AUG 2007	FEWSNET – excessively heavy rainfall resulted in flooding that inundated crops.
3	20-27 AUG 2007	CRED EM-DAT Disaster # 2007-0305 – 26 Jul – 10 Oct 2007 excessive rainfall
		caused flooding in Burkina Faso resulting in 52 deaths and 121,043 people
		affected DREE Pullatin MDRRE004 Heavy rains in Dayling Face since hasining of
		DREF Bulletin MDRBF004 – Heavy rains in Burkina Faso since beginning of
		August 2007 have led to flooding, marooned villages, and extensive damage to houses and infrastructure.
4	06-07 AUG 2001	
4	00-07 AUG 2001	Adeoye et al. (2009): Jigawa flood and windstorm resulted in 6 deaths and
		450,150 people displaced, while the Kano flood and wind storm resulted in 27
		deaths and 20,445 people displaced.
		CRED EM-DAT Disaster # 2001-0494 – Event help contribute to flash flooding
		event in northern Nigeria at the end of the month that resulted in a broken
	04.05.4110.2005	dam/burst bank resulting in 200 deaths and 84,065 people affected.
5	04-05 AUG 2007	FEWSNET – Excessive rainfall across Burkina Faso, Ivory Coast, and Ghana.
		Helped to increase Lake Volta lake levels.
		CRED EM-DAT Disaster # 2007-0305 – Event contributed to long term flooding
		in Burkina Faso that was reported in the region from 26 Jul – 10 Oct 2007 that
		resulted in 52 deaths and 121,043 people affected.
		CRED EM-DAT Disaster # 2007-0389 – Event partially indirectly contributed to
		long term flooding in Niger from 26 Jul – 10 Oct 2007 that resulted in 7 deaths
	*****	and 57,274 people affected.
6	23-24 AUG 2019	FEWSNET – abundant rains over the past week have resulted in flooding in
		western Niger and central Mali.
		CRED EM-DAT Disaster # 2019-0420 – Flooding from 24 Aug – 12 Sep 2019
_		affected 6,474 people in Mali.
7	01-02 SEP 2009	CRED EM-DAT Disaster # 2009-0523 – Partially contributed to the May – Sep
		2009 flooding of region that resulted in 25 deaths and 20,406 people affected in
		Mali.
8	19-20 JUL 2001	Adeoye et al. (2009): Zamfara flood resulted in buildings and farmland
		destroyed, 1 death, and 12,398 people affected, while the Sokoto flood and
		windstorm resulted in houses and farmland destroyed with 0 deaths, but 16,000
		people affected.
		CRED EM-DAT Disaster # 2001-0408 – Event contributed to the July 2001
		flooding event in northern Nigeria that affected 3,852 people.
9	14-15 JUL 2007	FEWSNET – Heavy rains in July have increased surface moisture over Wetern
		Burkina Faso and Mali.
		CRED EM-DAT Disaster # 2007-0275 – Event contributed to flooding during
		late July over Mali resulting in 9 deaths and 47,255 people affected.
10	19-20 JUL 2004	FEWSNET – Marked increase in rainfall over Mali and Burkina Faso at this
		time.

Table 3. Listing of the 4 different types of heavy rainfall events where the duration and peak intensity falls outside of \pm 0.5 standard deviation of the top 100 event mean

Longer duration/ weaker peak intensity	Longer duration/ higher peak intensity	Shorter duration/ weaker peak intensity	Shorter duration/ higher peak intensity
14 events	5 events	4 events	14 events
(3, 6, 9, 28, 35, 43,	(7, 14, 22, 32, 62)	(41, 76, 89, 93)	(1, 12, 13, 16, 47, 61,
50, 53, 55, 64, 65, 70,			66, 69, 75, 79, 81, 83,
84, 94)			92, 99)

1064	Figure Captions
1065	Figure 1. Top 100 event (a) locations of rainfall delivery within the analysis region (circles) and (b) the
1066	storm genesis locations (crosses). Color coding in (a) indicates the total rainfall amount, and in (b) the
1067	storm genesis locations associated with the Mali (blue), Burkina Faso (red), and northern Nigeria (purple)
1068	clusters. Shading in both panels denotes the topography in meters.
1069	
1070	Figure 2. (a) 24-h maximum total rainfall (mm) for the top 100 events shown in Fig. 1, as well as their (b)
1071	seasonal distribution (blue bars) and the IMERG climatological monthly precipitation (red line; mm day-1)
1072	area-averaged over the analysis region box shown in Fig. 1.
1073	
1074	
1075	Figure 3. Spatial area of the total 12Z-12Z daily rainfall (× 10 ³ km ²) for the top 100 events starting at 100
1076	mm threshold for the events listed in Table 1.
1077	
1078	Figure 4. (a) Climatological 12Z precipitable water (PWAT; shaded; mm) and 925 hPa horizontal winds
1079	(vectors; m s ⁻¹), and their (b) 12Z composite anomalies for the top 100 events. (c) Climatological 12Z 600
1080	hPa – 925 hPa horizontal wind difference (vectors; m s ⁻¹) and magnitude (shaded; m s ⁻¹) and their (d) 122
1081	composite anomalies. Stippling and bold vectors in (b) and (d) indicate values significant at the 95% leve
1082	of confidence. Box indicates the defined West African Sahel region.
1083	
1084	Figure 5. Top 10 events, and the corresponding 24-h rainfall totals (mm). Red circle denotes location of
1085	maximum 24-h rainfall for each event.
1086	
1087	Figure 6. Diurnal cycle of precipitation (mm hr ⁻¹) of the top 10 events. Total 24 h rainfall amount and
1088	duration for each event based on the 10 mm/day rainfall threshold is provided. Gray line denotes the time
1089	of maximum rainfall intensity at the maximum 24-h total rainfall location

1090	
1091	Figure 7. (a) Diurnal cycle of rainfall (mm h ⁻¹) of the identified longer duration/weaker peak intensity cases
1092	(14 events) and their composite mean (red). (b) Location of the maximum 24-hr rainfall total for each of
1093	the 14 events. (c) and (d) are the same as (a) and (b) respectively, but for the identified shorter duration/
1094	higher peak intensity cases (14 events).
1095	
1096	Figure 8. Tracking of the MCS convective core defined by the 100 mm/day rain shield that traverses the
1097	site of maximum 24-h rainfall (red circle) for each event. Green (blue) marks denote location of the
1098	convective core for times prior (after) the peak intensity as defined by the gray lines in Fig. 6. The estimated
1099	distance (km) is provided.
1100	
1101	Figure 9. Storm area (×10 ³ km ²) for the 5 mm day ⁻¹ (black) and 500 mm day ⁻¹ (blue) rain shields for the
1102	top 10 events. Gray line denotes time of maximum rainfall intensity at the maximum 24-h total rainfall
1103	location.
1104	
1105	Figure 10. (a) 700 hPa geopotential height (contours; m), 700 hPa wind (vectors; m s ⁻¹), and precipitable
1106	water (shading; mm) anomalies, and (b) $600 \text{ hPa} - 925 \text{ hPa}$ horizontal wind difference (vectors; m s ⁻¹) and
1107	magnitude (shaded; m s) at 18Z 20 August 2019 for CASE01. (c) & (d) similar, but at 00Z 27 August 2007
1108	for CASE03. (e) & (f) similar to (a) & (b), but at 00Z 24 August 2019 for CASE06. Red circle denotes the
1109	location of the event maximum rainfall, while red dashed lined denotes position of the Sahel/tropical Africa
1110	dryline boundary as inferred from the 925 hPa specific humidity field.
1111	
1112	Figure 11. Hovmöllers of (left column) 700 hPa relative vorticity ($\times 10^{-5} s^{-1}$) averaged from 10°N - 15°N,
1113	and (right column) precipitable water differences from the 2000-2019 climatology (mm) averaged from
1114	10°N - 15°N for the (a & b) CASE01, (c & d) CASE03, and (e & f) CASE06 events. The circle denotes

1115 the time and longitude of the peak intensity of the event, while dashed lines denote relevant wave 1116 disturbances and their estimated speeds as indicated from the 700 hPa relative vorticity field. 1117 1118 Figure 12. (a) 700 hPa geopotential height (contours; m), 700 hPa wind (vectors; m s⁻¹), and precipitable 1119 water (shading; mm) anomalies, and (b) 600 hPa – 925 hPa horizontal wind difference (vectors; m s⁻¹) and 1120 1121 magnitude (shaded; m s⁻¹) at 12Z 7 August 2012 for CASE02. (c) & (d) similar, but at 00Z 2 September 2009 for CASE07. (e) & (f) similar to (a) & (b), but at 2Z 20 July 2004 for CASE10. Red circle denotes 1122 the location of the event maximum rainfall, while red dashed lined denotes position of the Sahel/tropical 1123 Africa dryline boundary as inferred from the 925 hPa specific humidity field. 1124 1125 1126 Figure 13. Hovmöllers of (left column) 700 hPa relative vorticity (×10⁻⁵ s⁻¹) averaged from 10°N - 15°N, and (right column) precipitable water differences from the 2000-2019 climatology (mm) averaged from 1127 10°N - 15°N for the (a & b) CASE02, (c & d) CASE07, and (e & f) CASE10 events. The circle denotes 1128 the time and longitude of the peak intensity of the event, while dashed lines denote relevant wave 1129 disturbances and their estimated speeds as indicated from the 700 hPa relative vorticity field. 1130 1131 Figure 14. (a) 700 hPa geopotential height (contours; m), 700 hPa wind (vectors; m s⁻¹), and precipitable 1132 water (shading; mm) anomalies, and (b) 600 hPa - 925 hPa horizontal wind difference (vectors; m s⁻¹) and 1133 magnitude (shaded; m s⁻¹) at 15Z 6 August 2001 for CASE04. (c) & (d) similar, but at 00Z 5 August 2007 1134 for CASE05. (e) & (f) similar to (a) & (b), but at 15Z 19 July 2001 for CASE08. (g) & (h) similar to (a) & 1135 1136 (b), but at 18Z 14 July 2007 for CASE09. Red circle denotes the location of the event maximum rainfall,

while red dashed lined denotes position of the Sahel/tropical Africa dryline boundary as inferred from the

1139

1137

1138

925 hPa specific humidity field.

Figure 15. Hovmöllers of (left column) 700 hPa relative vorticity (×10⁻⁵ s⁻¹) averaged from 10°N - 15°N, and (right column) precipitable water differences from the 2000-2019 climatology (mm) averaged from 10°N - 15°N for the (a & b) CASE04, (c & d) CASE05, (e & f) CASE08, and (g & h) CASE09 events. The circle denotes the time and longitude of the peak intensity of the event, while dashed lines denote relevant wave disturbances and their estimated speeds as indicated from the 700 hPa relative vorticity field.

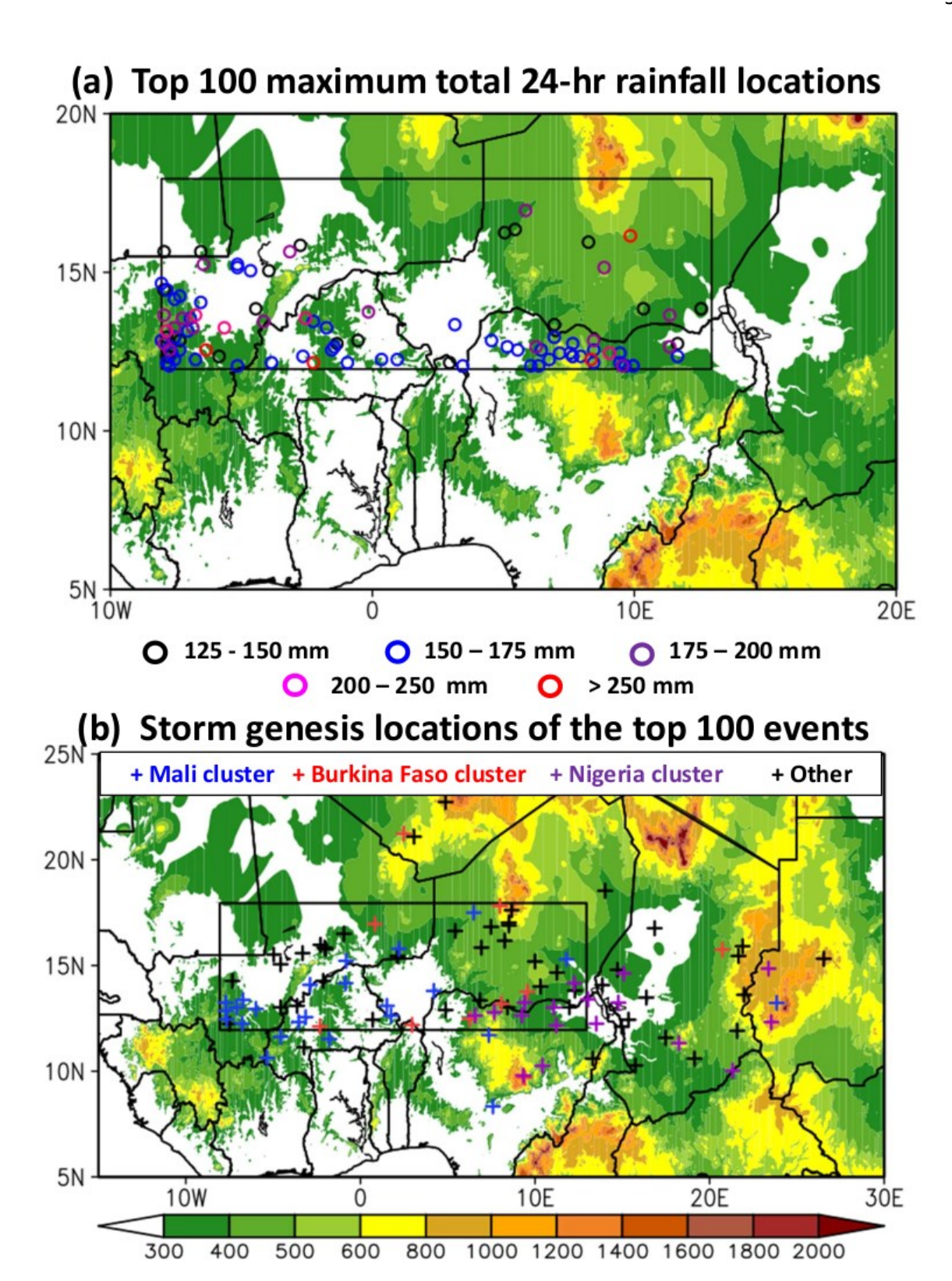


Figure 1. Top 100 event (a) locations of rainfall delivery within the analysis region (circles) and (b) the storm genesis locations (crosses). Color coding in (a) indicates the total rainfall amount, and in (b) the storm genesis locations associated with the Mali (blue), Burkina Faso (red), and northern Nigeria (purple) clusters. Shading in both panels denotes the topography in meters.

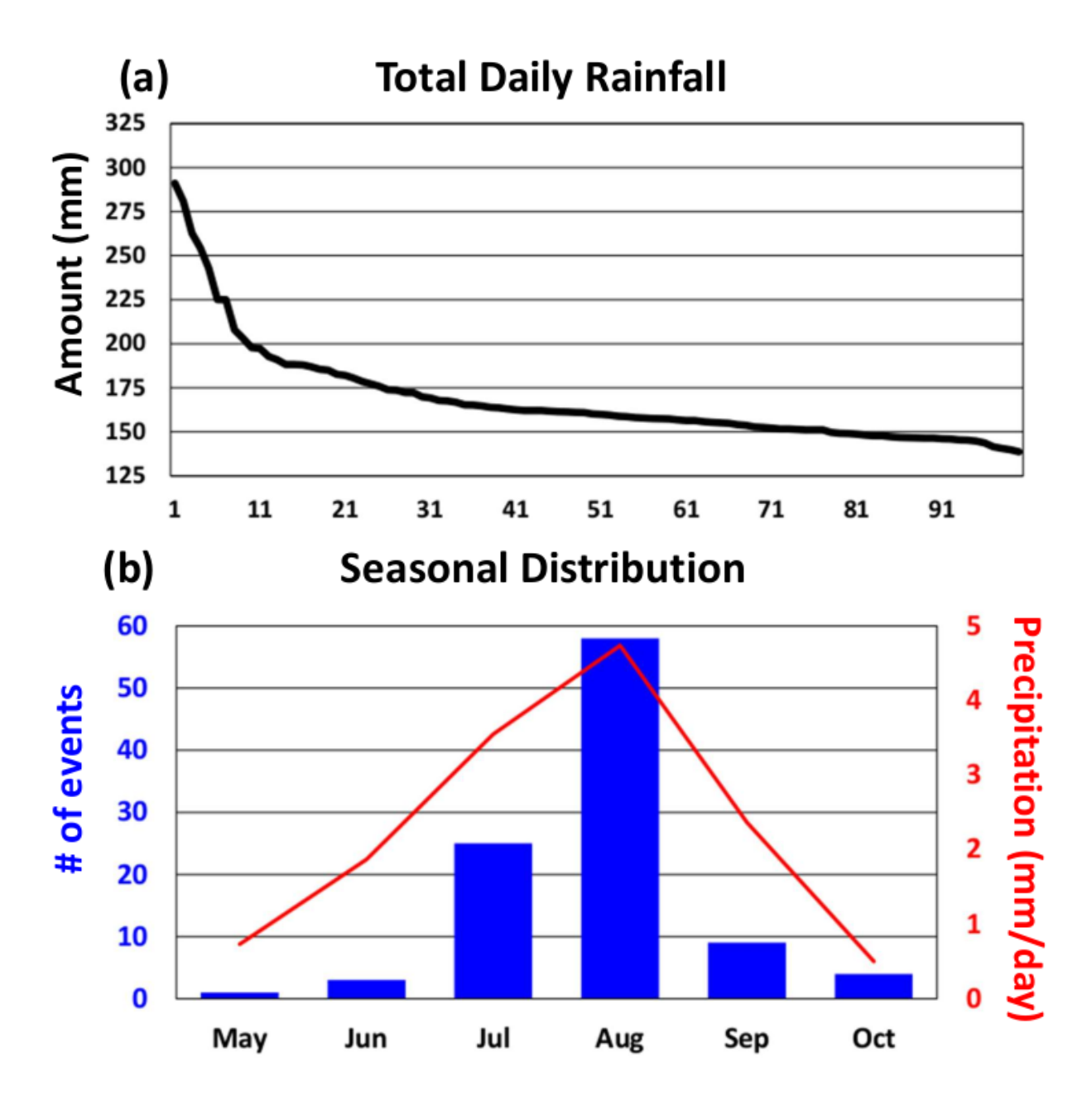


Figure 2. (a) 24-h maximum total rainfall (mm) for the top 100 events shown in Fig. 1, as well as their (b) seasonal distribution (blue bars) and the IMERG climatological monthly precipitation (red line; mm day⁻¹) area-averaged over the analysis region box shown in Fig. 1.

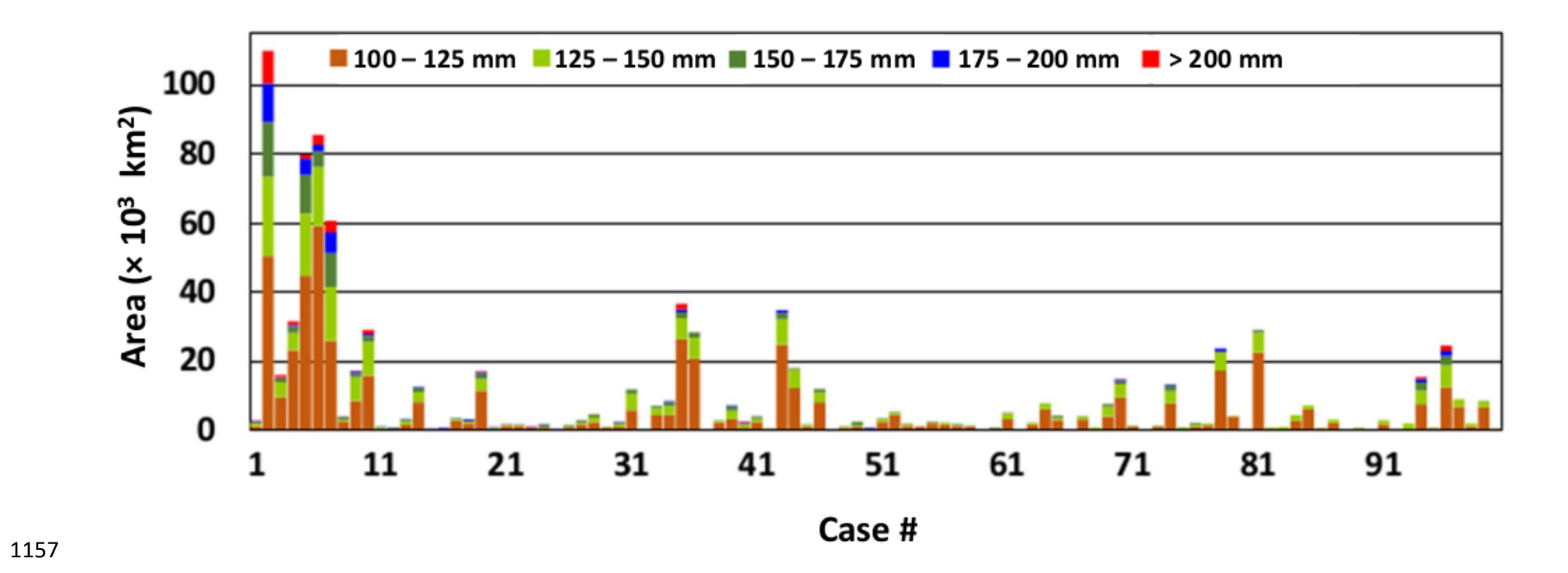


Figure 3. Spatial area of the total 12Z-12Z daily rainfall (\times 10³ km²) for the top 100 events starting at 100 mm threshold for the events listed in Table 1.

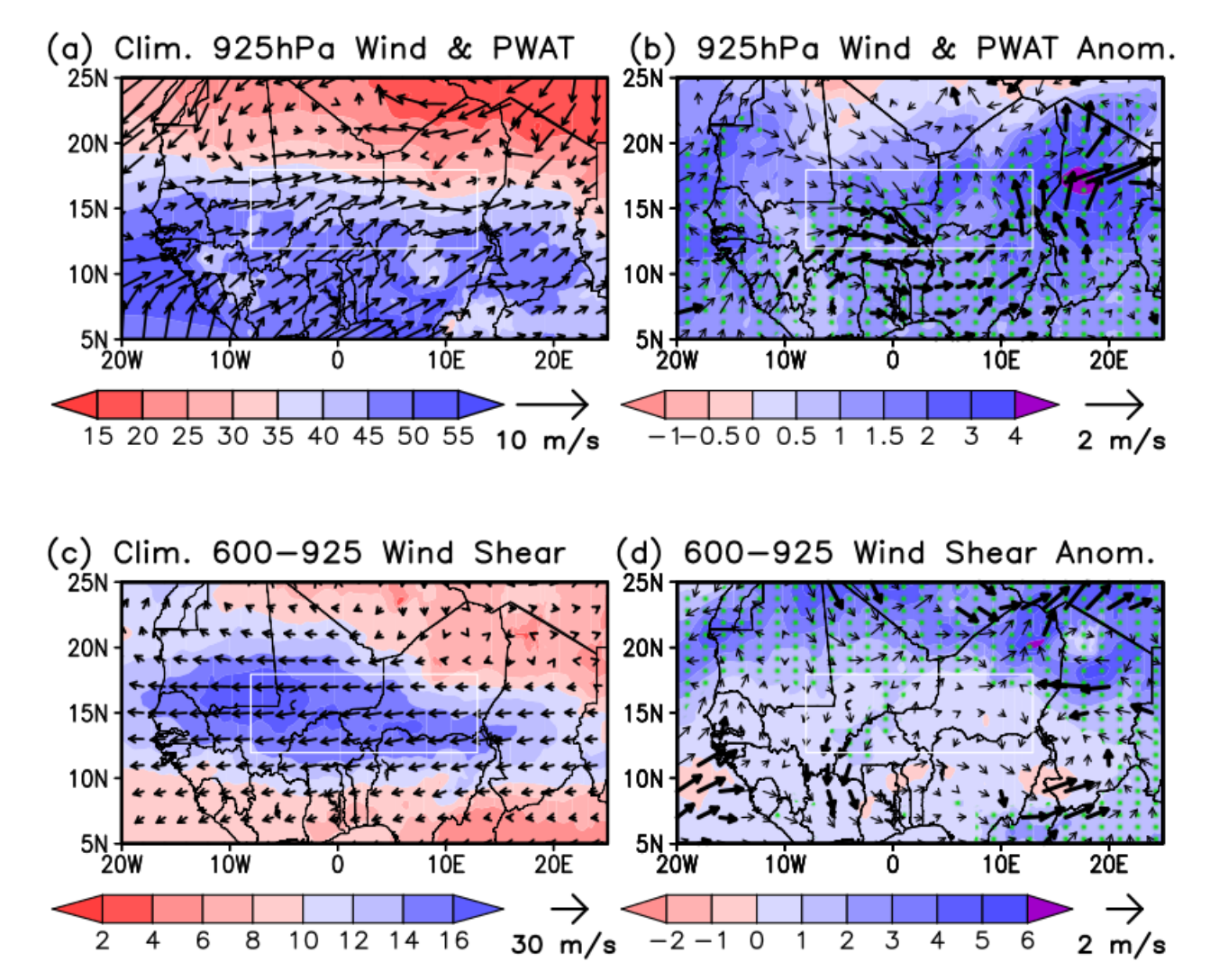


Figure 4. (a) Climatological 12Z precipitable water (PWAT; shaded; mm) and 925 hPa horizontal winds (vectors; m s⁻¹), and their (b) composite 12Z anomalies for the top 100 events. (c) Climatological 12Z 600 hPa – 925 hPa horizontal wind difference (vectors; m s⁻¹) and magnitude (shaded; m s⁻¹) and their (d) 12Z composite anomalies. Stippling and bold vectors in (b) and (d) indicate values significant at the 95% level of confidence. Box indicates the defined West African Sahel region.

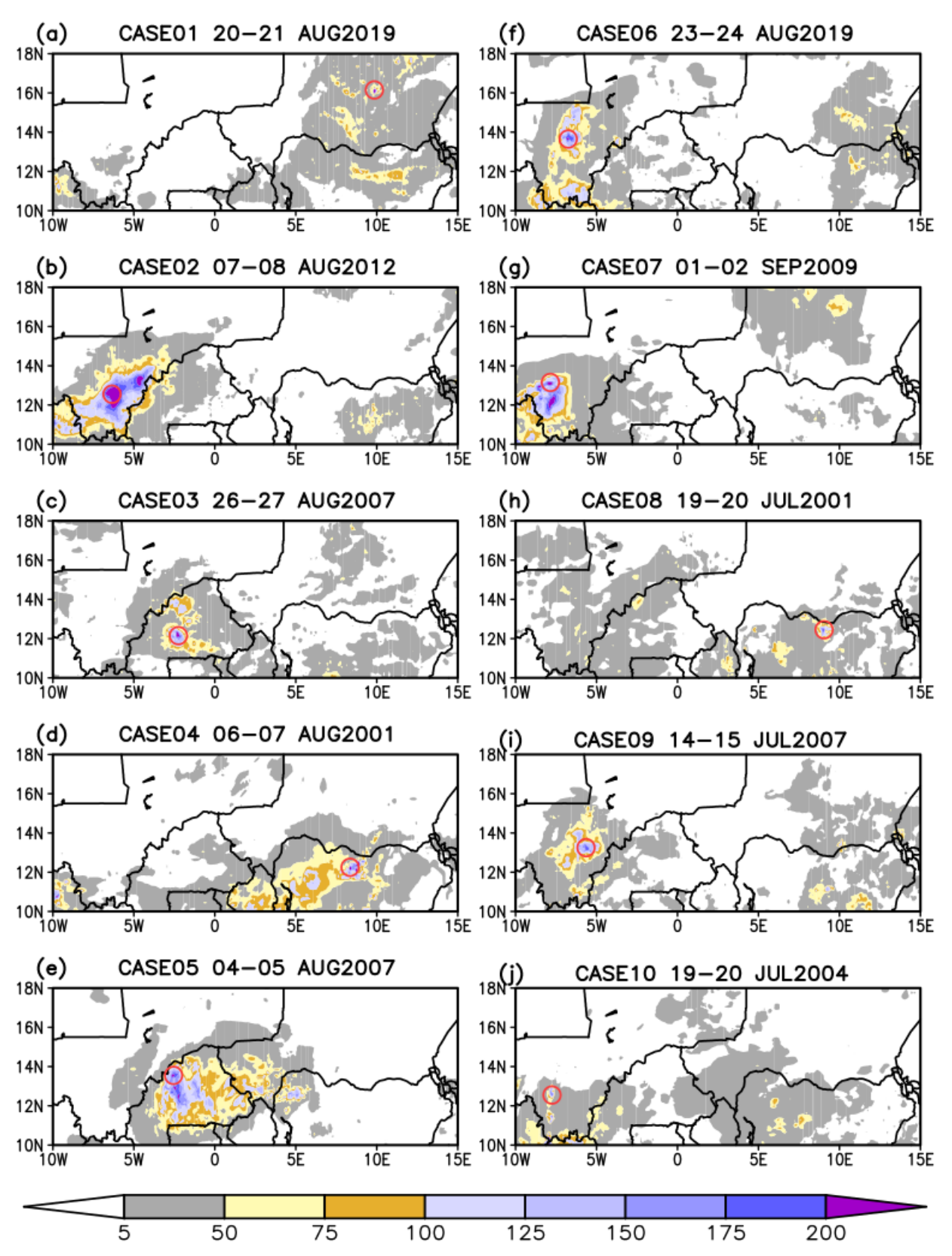


Figure 5. Top 10 events, and their corresponding 24-h rainfall totals (mm). Red circle denotes location of maximum 24-h rainfall for each event.

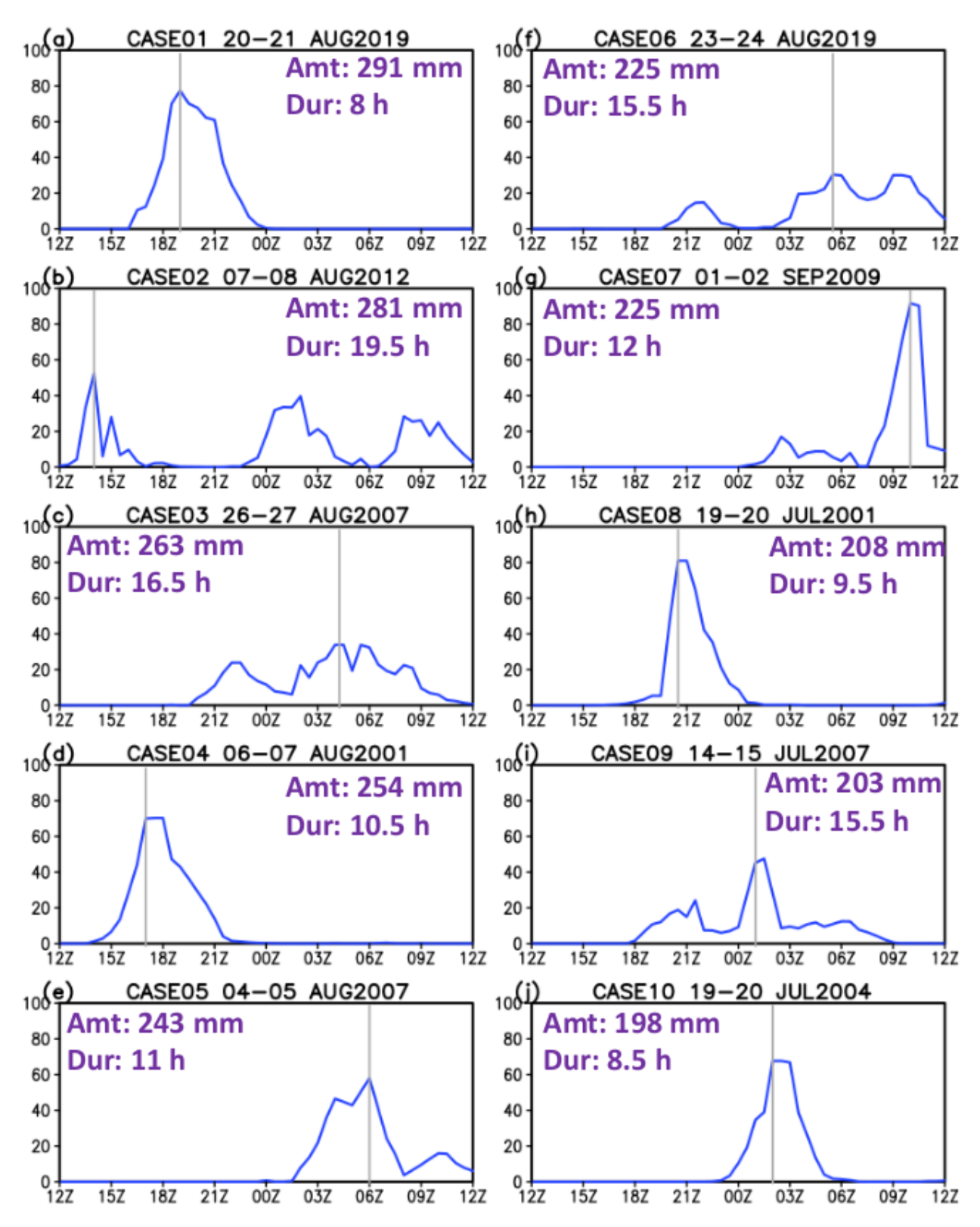


Figure 6. Diurnal cycle of precipitation (mm hr⁻¹) of the top 10 events. Total 24 h rainfall amount and duration for each event based on the 10 mm/day rainfall threshold is provided. Gray line denotes the time of maximum rainfall intensity at the maximum 24-h total rainfall location.

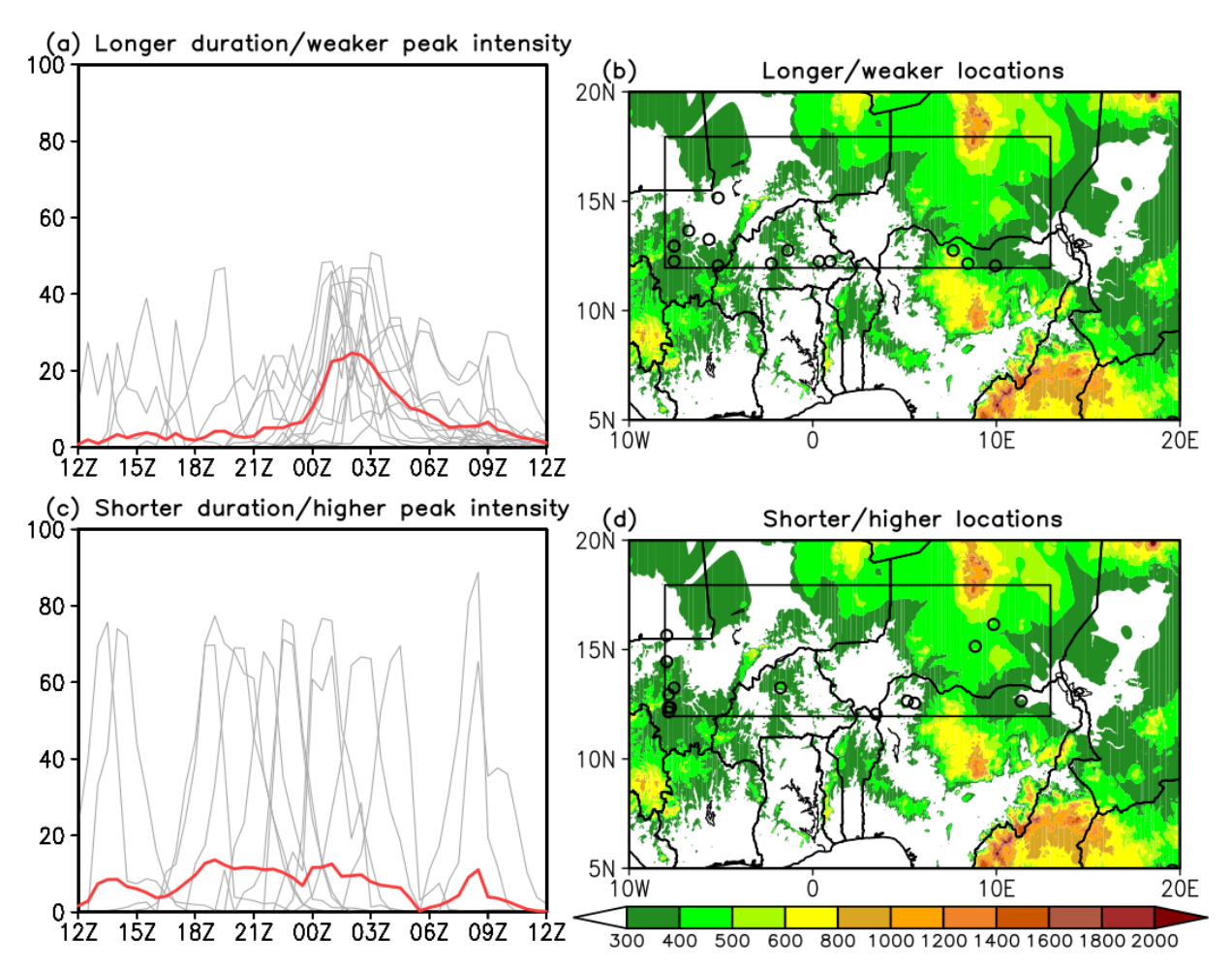


Figure 7. (a) Diurnal cycle of rainfall (mm h⁻¹) of the identified longer duration/weaker peak intensity cases (14 events) and their composite mean (red). (b) Location of the maximum 24-hr rainfall total for each of the 14 events. (c) and (d) are the same as (a) and (b) respectively, but for the identified shorter duration/higher peak intensity cases (14 events).

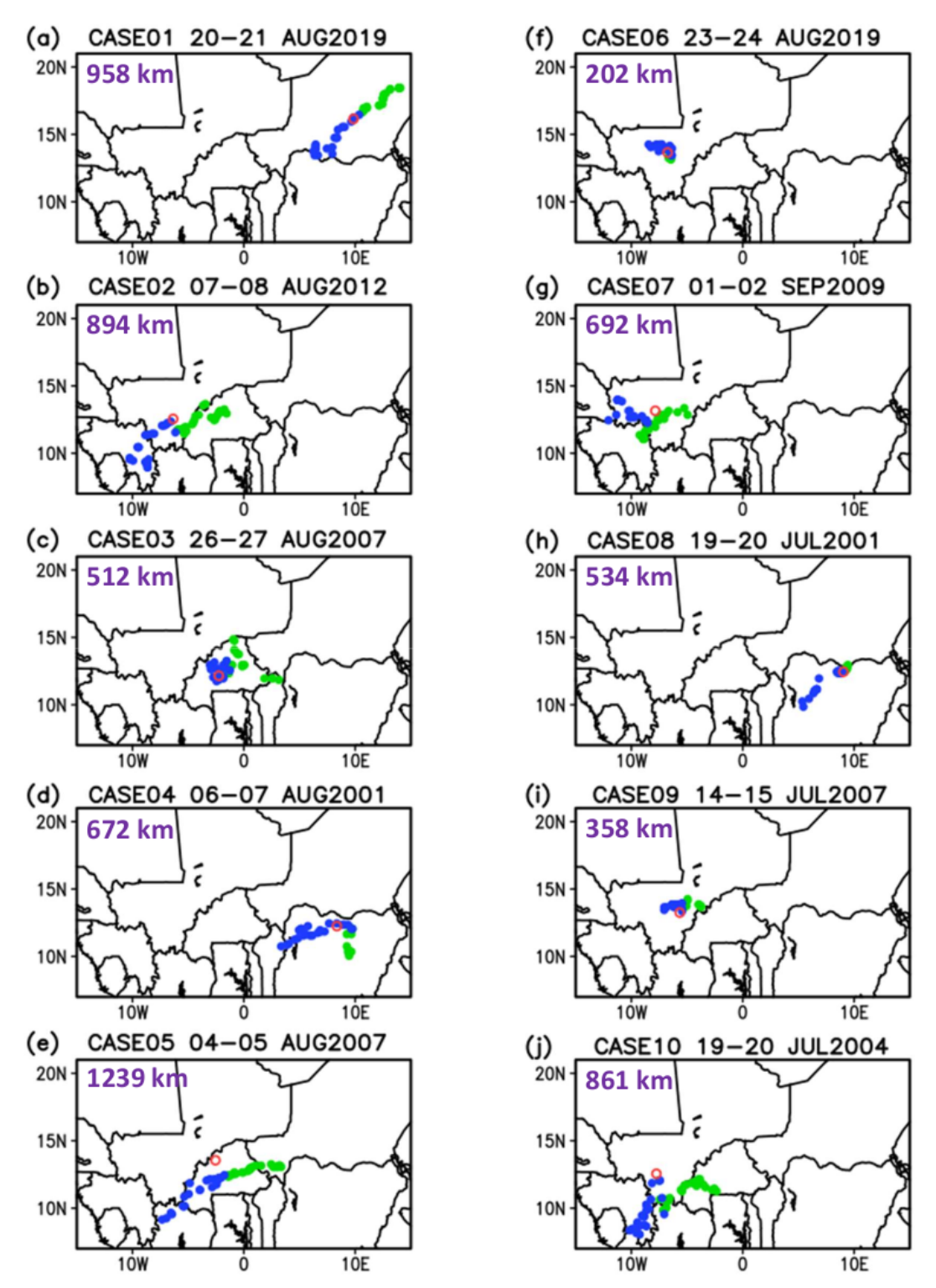


Figure 8. Tracking of the MCS convective core defined by the 100 mm/day rain shield that traverses the site of maximum 24-h rainfall (red circle) for each event. Green (blue) marks denote location of the convective core for times prior (after) the peak intensity as defined by the gray lines in Fig. 6. The estimated distance (km) is provided.

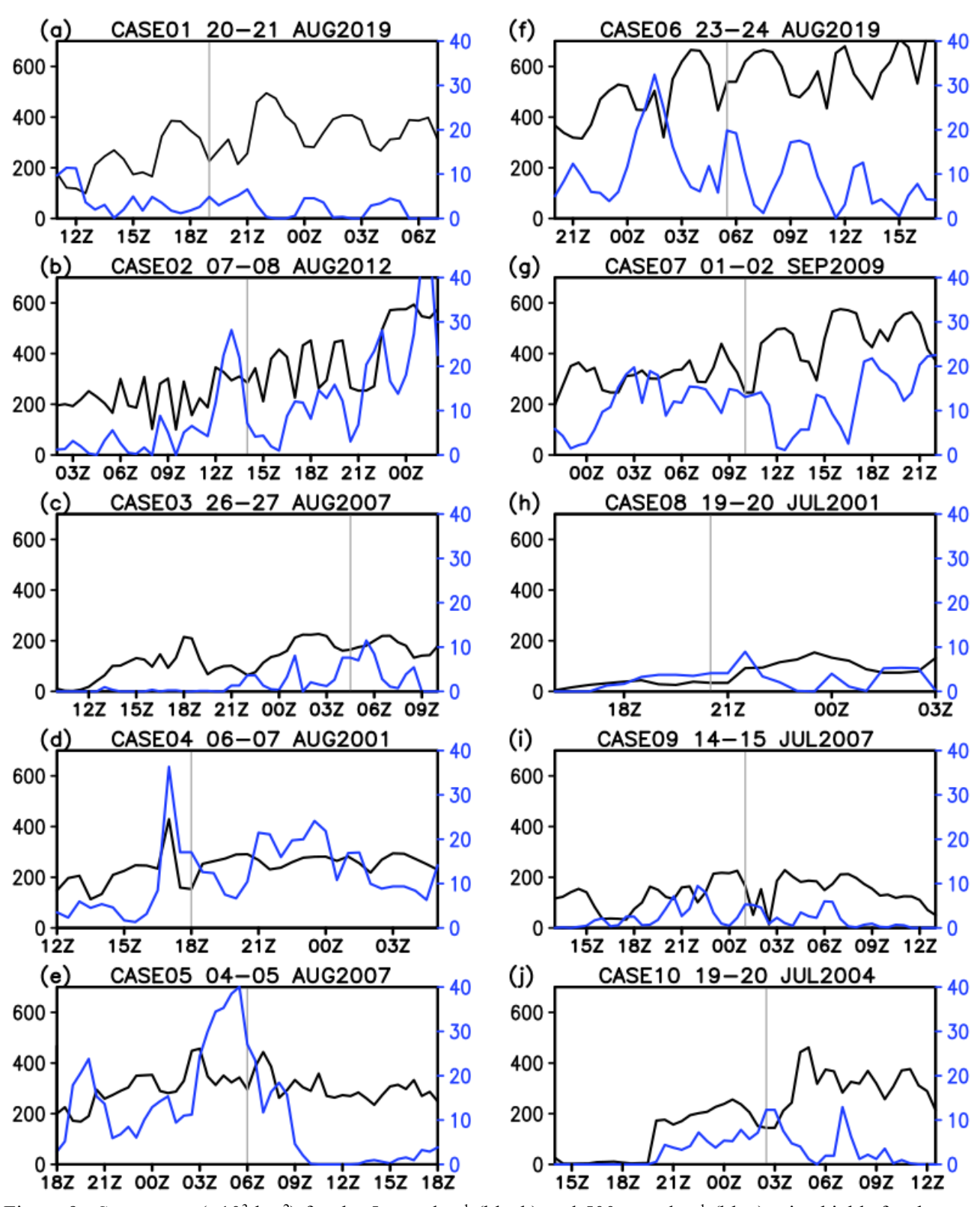


Figure 9. Storm area ($\times 10^3$ km²) for the 5 mm day⁻¹ (black) and 500 mm day⁻¹ (blue) rain shields for the top 10 events. Gray line denotes time of maximum rainfall intensity at the maximum 24-h total rainfall location.

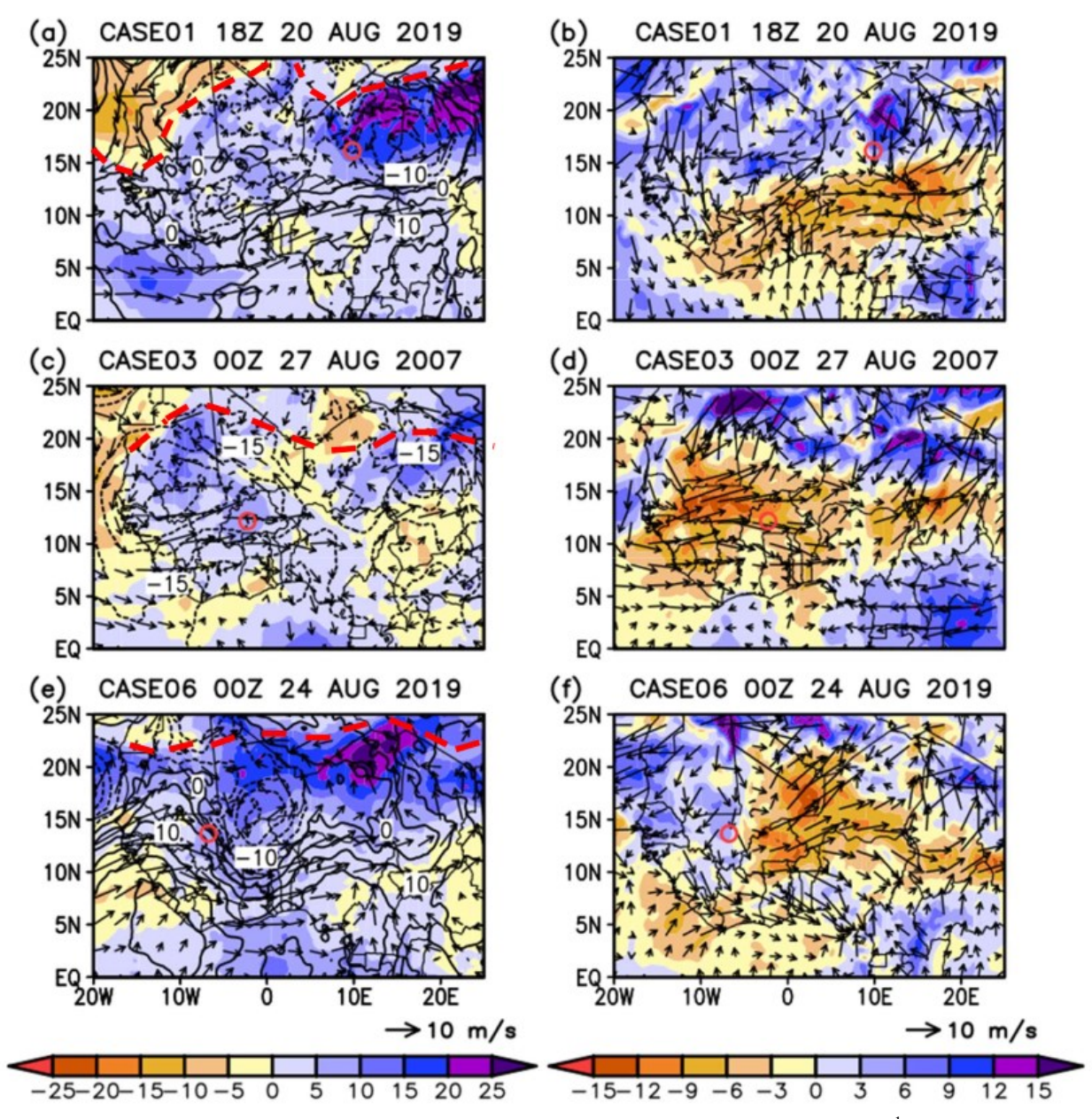


Figure 10. (a) 700 hPa geopotential height (contours; m), 700 hPa wind (vectors; m s⁻¹), and precipitable water (shading; mm) anomalies, and (b) 600 hPa – 925 hPa horizontal wind difference (vectors; m s⁻¹) and magnitude (shaded; m s) at 18Z 20 August 2019 for CASE01. (c) & (d) similar, but at 00Z 27 August 2007 for CASE03. (e) & (f) similar to (a) & (b), but at 00Z 24 August 2019 for CASE06. Red circle denotes the location of the event maximum rainfall, while red dashed lined denotes position of the Sahel/tropical Africa dryline boundary as inferred from the 925 hPa specific humidity field.

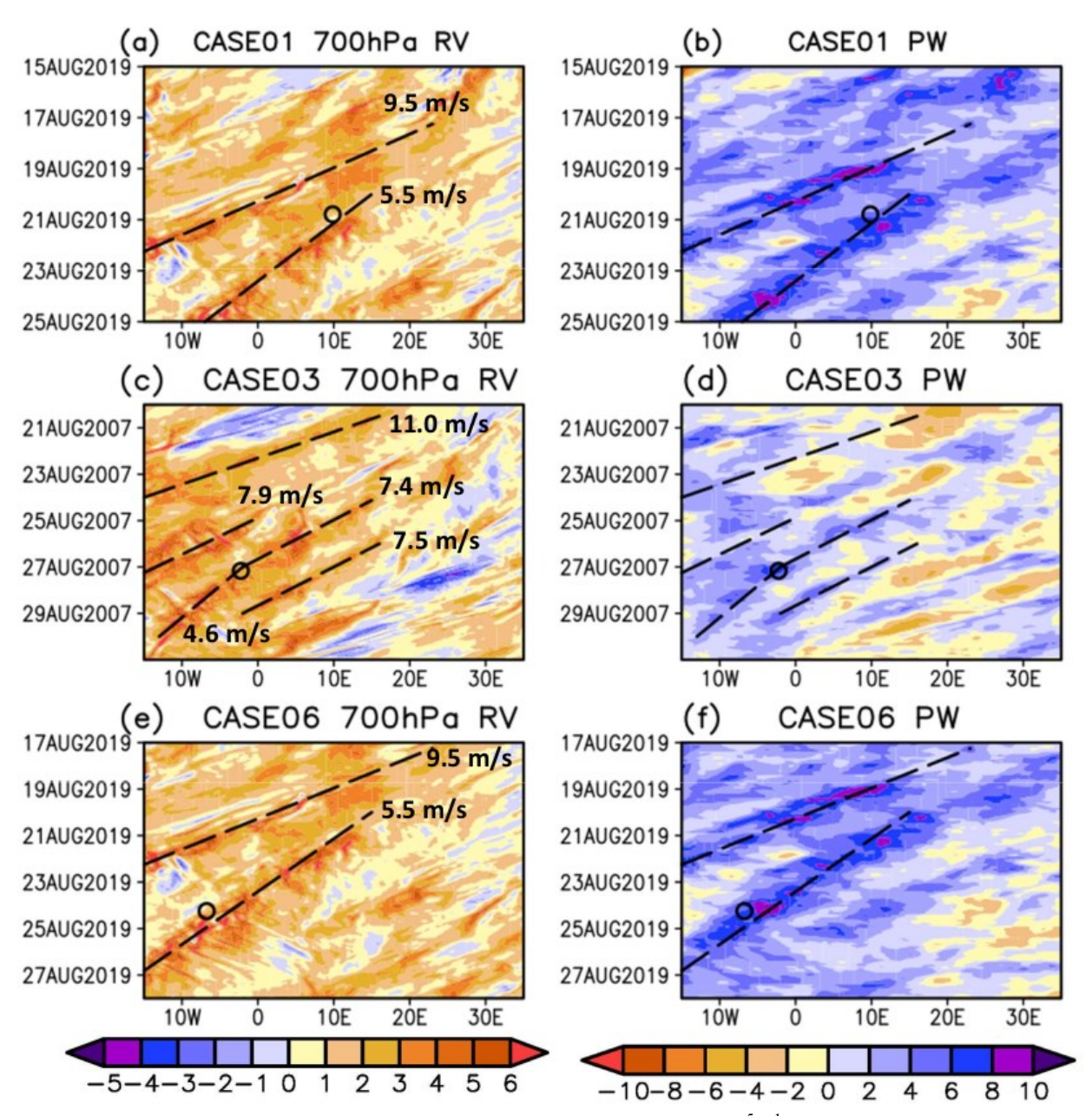


Figure 11. Hovmöllers of (left column) 700 hPa relative vorticity ($\times 10^{-5}\,\mathrm{s}^{-1}$) averaged from 10°N - 15°N, and (right column) precipitable water differences from the 2000-2019 climatology (mm) averaged from 10°N - 15°N for the (a & b) CASE01, (c & d) CASE03, and (e & f) CASE06 events. The circle denotes the time and longitude of the peak intensity of the event, while dashed lines denote relevant wave disturbances and their estimated speeds as indicated from the 700 hPa relative vorticity field.

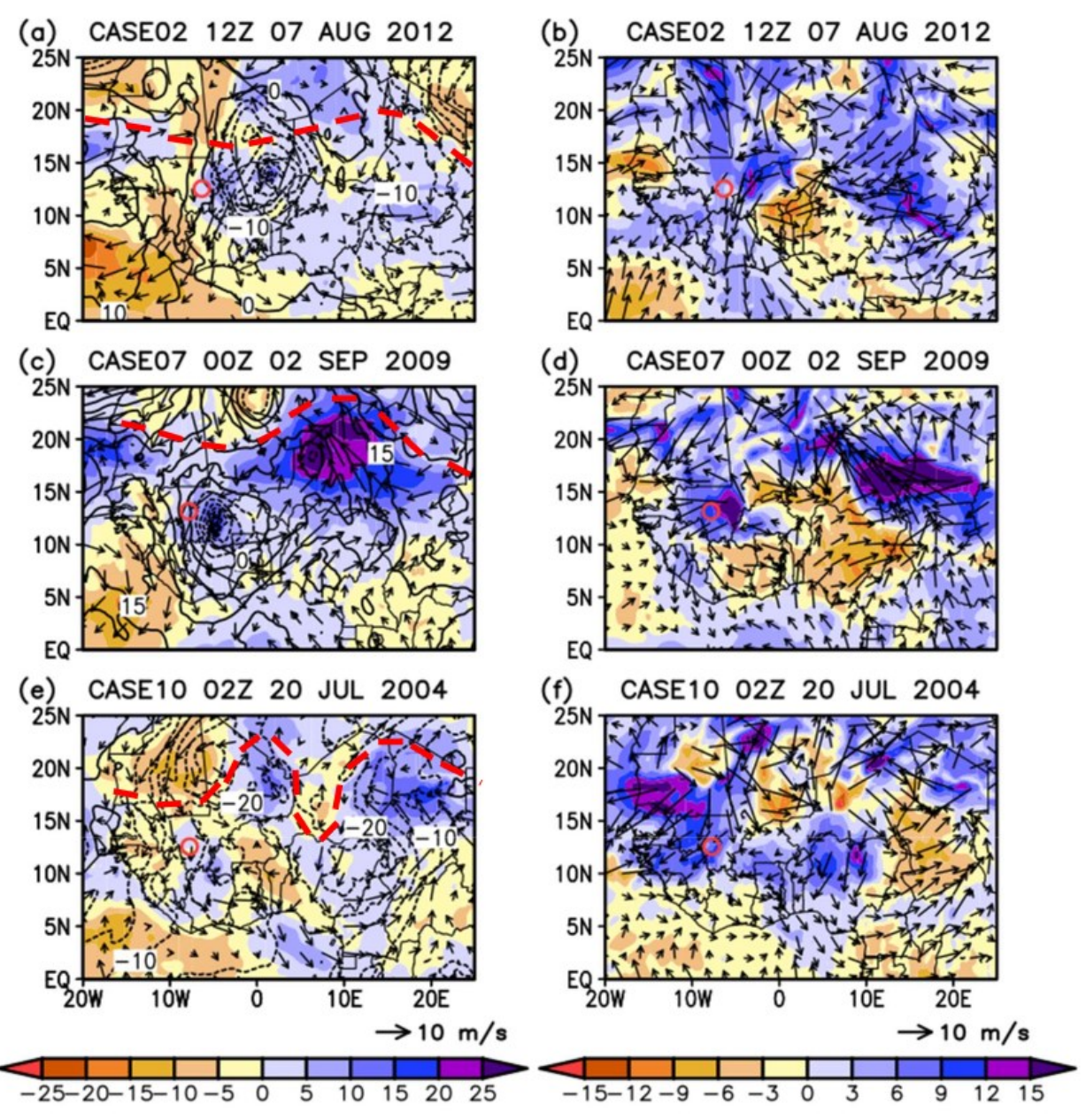


Figure 12. (a) 700 hPa geopotential height (contours; m), 700 hPa wind (vectors; m s⁻¹), and precipitable water (shading; mm) anomalies, and (b) 600 hPa – 925 hPa horizontal wind difference (vectors; m s⁻¹) and magnitude (shaded; m s⁻¹) at 12Z 7 August 2012 for CASE02. (c) & (d) similar, but at 00Z 2 September 2009 for CASE07. (e) & (f) similar to (a) & (b), but at 2Z 20 July 2004 for CASE10. Red circle denotes the location of the event maximum rainfall, while red dashed lined denotes position of the Sahel/tropical Africa dryline boundary as inferred from the 925 hPa specific humidity field.

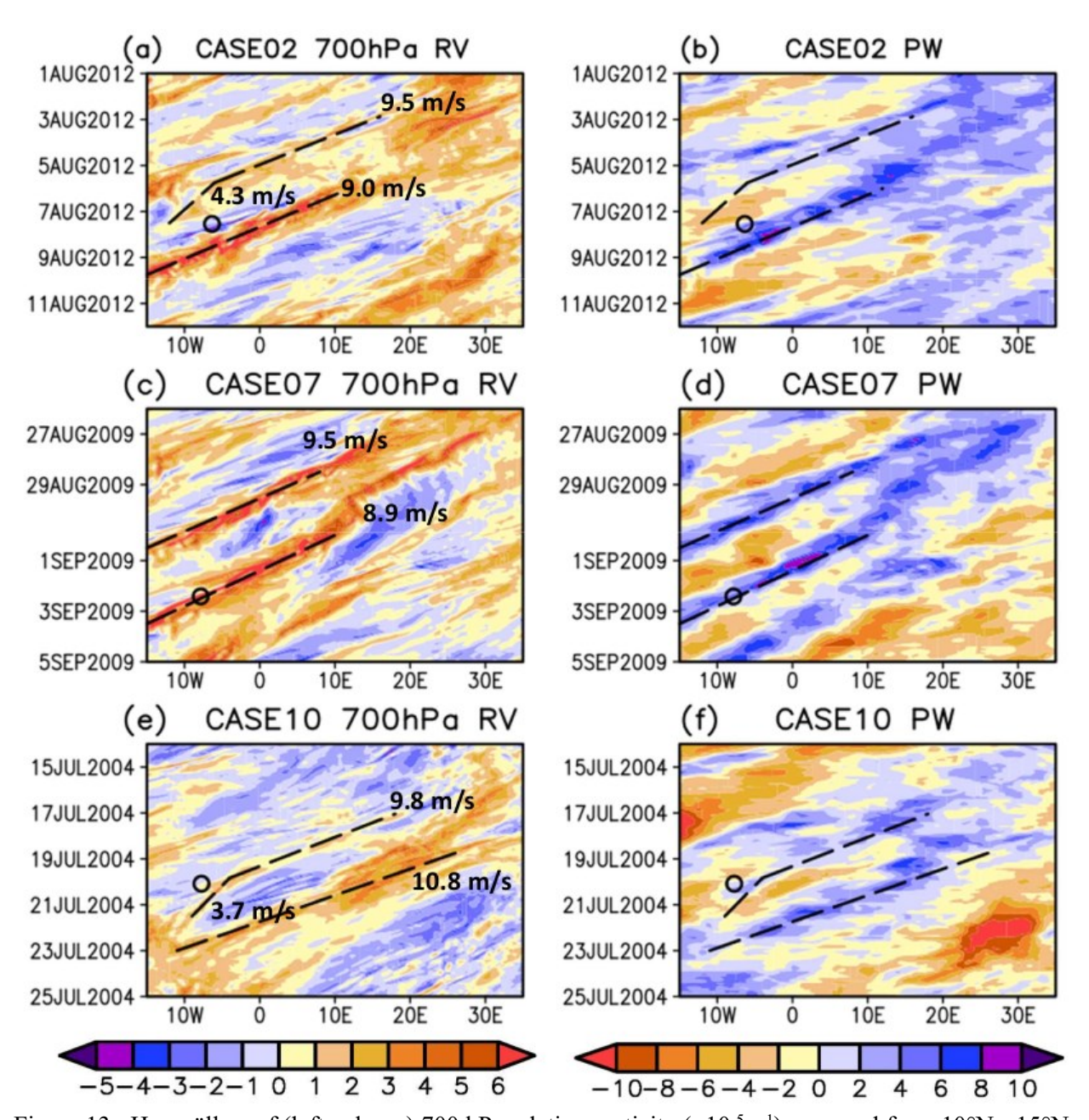


Figure 13. Hovmöllers of (left column) 700 hPa relative vorticity (×10⁻⁵ s⁻¹) averaged from 10°N - 15°N, and (right column) precipitable water differences from the 2000-2019 climatology (mm) averaged from 10°N - 15°N for the (a & b) CASE02, (c & d) CASE07, and (e & f) CASE10 events. The circle denotes the time and longitude of the peak intensity of the event, while dashed lines denote relevant wave disturbances and their estimated speeds as indicated from the 700 hPa relative vorticity field.

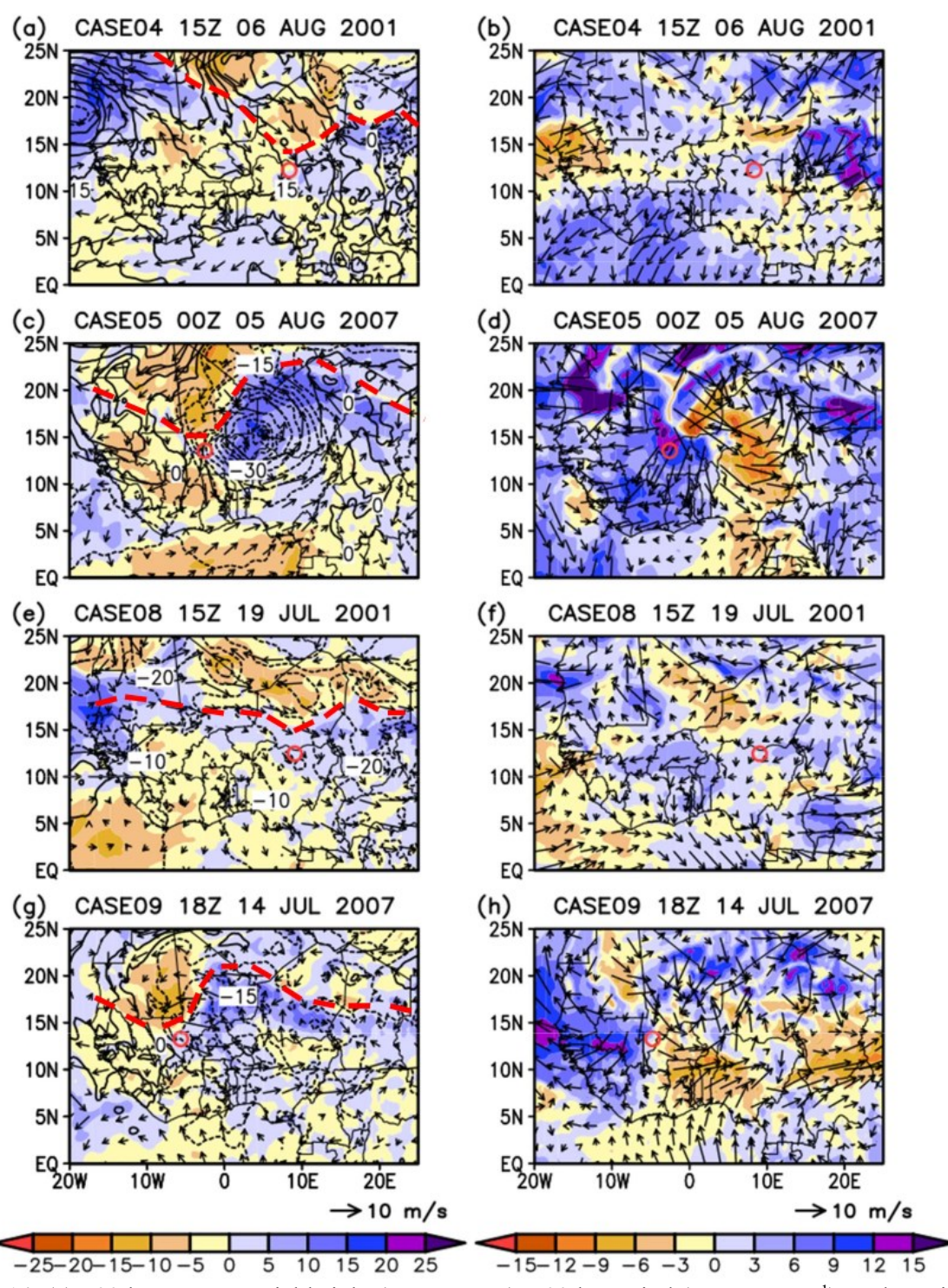


Figure 14. (a) 700 hPa geopotential height (contours; m), 700 hPa wind (vectors; m s⁻¹), and precipitable water (shading; mm) anomalies, and (b) 600 hPa – 925 hPa horizontal wind difference (vectors; m s⁻¹) and magnitude (shaded; m s⁻¹) at 15Z 6 August 2001 for CASE04. (c) & (d) similar, but at 00Z 5 August 2007 for CASE05. (e) & (f) similar to (a) & (b), but at 15Z 19 July 2001 for CASE08. (g) & (h) similar to (a) & (b), but at 18Z 14 July 2007 for CASE09. Red circle denotes the location of the event maximum rainfall, while red dashed lined denotes position of the Sahel/tropical Africa dryline boundary as inferred from the 925 hPa specific humidity field.

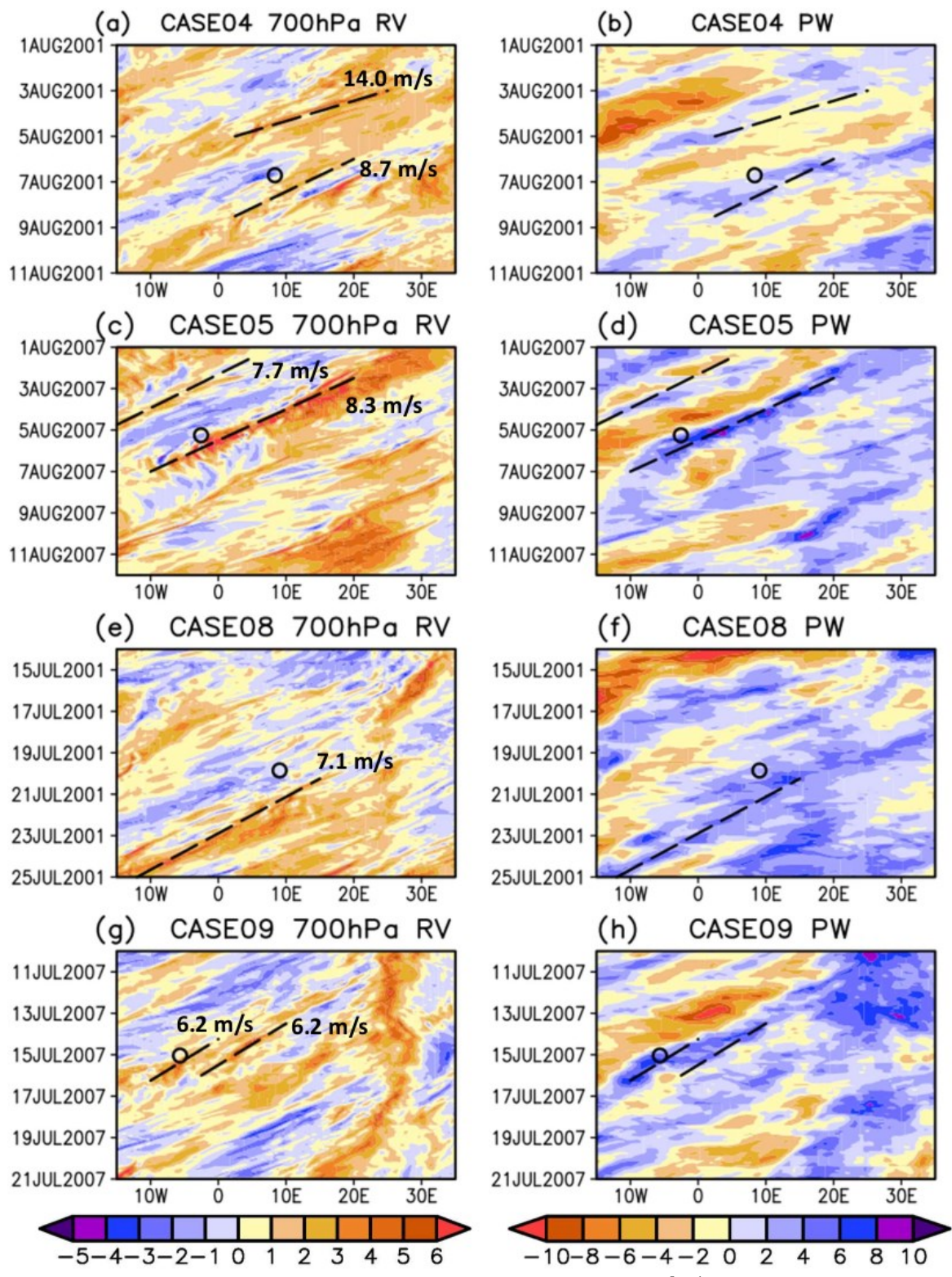


Figure 15. Hovmöllers of (left column) 700 hPa relative vorticity ($\times 10^{-5}$ s⁻¹) averaged from 10°N - 15°N, and (right column) precipitable water differences from the 2000-2019 climatology (mm) averaged from 10°N - 15°N for the (a & b) CASE04, (c & d) CASE05, (e & f) CASE08, and (g & h) CASE09 events. The circle denotes the time and longitude of the peak intensity of the event, while dashed lines denote relevant wave disturbances and their estimated speeds as indicated from the 700 hPa relative vorticity field.